fluids

MDPI

Article

Quantitative Sensitivity Analysis of Key Parameters in Impellers of Vane-Type Mixed-Flow Pumps Under High Gas Content Conditions

Minghao Zhou [1,2,*], Guangtai Shi [1,2], Yuanbo Shi [1,2] and Peng Li [1,2]

[1] Laboratory of Fluid Machinery and Engineering, Xihua University, Chengdu 610039, China
[2] School of Energy and Power Engineering, Xihua University, Chengdu 610039, China
* Correspondence: 15983566203@163.com

Abstract

Gas–liquid multiphase pumps are essential for deep-sea oil and gas production; however, their performance is severely limited under high gas volume fraction (GVF > 30%) conditions due to inefficient energy transfer and flow instability. In this study, a hybrid sensitivity analysis framework combining the Morris screening method and Sobol global sensitivity analysis is developed to quantitatively investigate the effects of impeller geometric parameters on pump performance at a GVF of 80%. Euler–Euler two-phase CFD simulations coupled with Python-based automated sampling are employed. The results show that the impeller outer diameter, axial length, and blade wrap angle are the three most influential parameters. The impeller outer diameter contributes 35.7% to the pressure rise, while an axial length exceeding 44 mm induces axial backflow and reduces efficiency by 8.2%. A critical wrap angle of 114° is identified for gas–liquid energy distribution, beyond which large-scale gas vortices intensify flow instability. Based on these findings, a hierarchical optimization strategy is proposed, resulting in a 6.8% improvement in efficiency and a 12.3% increase in pressure rise.

Keywords: gas–liquid multiphase pump; high gas volume fraction; sensitivity analysis; parameter interaction; impeller optimization

1. Introduction

Gas–liquid multiphase pumps are key equipment for the green development of deep-sea oil and gas resources. Recent experimental research has further shown that the energy performance and unsteady gas-liquid flow characteristics of multiphase rotodynamic pumps are strongly affected by gas–liquid interactions and operating conditions [1]. Their operational stability under ultra-high gas volume fraction (GVF > 80%) conditions directly determines the energy consumption and economic performance of subsea pipeline systems. Unlike conventional single-phase pumps, multiphase pumps involve complex interphase interactions, such as bubble breakup and gas-phase aggregation. The non-uniform bubble model (NUBM) proposed by Zhang et al. [2] further revealed that when the inlet gas volume fraction (IGVF) exceeds 15%, the ratio of virtual mass force to drag force increases by nearly 80%, leading to a reduction in energy transfer efficiency of more than 40% [3]. In particular, when the IGVF exceeds a critical threshold, periodic gas-cluster shedding at the impeller outlet induces strong pressure pulsations, posing a serious threat to system safety [4]. Consequently, suppressing flow instability under high-GVF conditions

Check for updates

Academic Editor: Tomoaki Kunugi

Received: 5 January 2026
Revised: 27 February 2026
Accepted: 19 March 2026
Published: 25 March 2026

Copyright: © 2026 by the authors. Licensee MDPI, Basel, Switzerland. This article is an open access article distributed under the terms and conditions of the Creative Commons Attribution (CC BY) license.

through impeller structural optimization has become a critical scientific challenge in oil and gas transportation.

From a fundamental fluid-dynamics perspective, flow characteristics are strongly governed by the Reynolds number, which distinguishes laminar, transitional, and turbulent regimes [5]. Since Reynolds' pioneering work on velocity decomposition, this concept has been widely applied to turbulent flows, multiphase systems, and complex engineering configurations. However, under high Reynolds number and multiphase conditions, accurate prediction of flow behaviour remains a major computational challenge, particularly in complex geometries and highly turbulent environments. Experimental studies have provided important insights into gas-phase accumulation mechanisms. Li et al. [6] observed through high-speed photography that the bubble number density near the impeller inlet shroud is three to five times higher than that in the central region. This phenomenon was further confirmed by Shi et al. [7–9], who reported that the tip leakage vortex (TLV) structure becomes discontinuous when the GVF exceeds 25%. Although the spatiotemporal evolution of gas-phase aggregation has been experimentally characterized [10], most existing studies remain limited to IGVF values below 30% [11]. Similar interfacial and multiphase interaction phenomena have also been reported in droplet-impact and liquid–liquid systems, where fluid viscosity and interfacial properties strongly influence flow structures and energy dissipation mechanisms [12].

From a numerical perspective, while the NUBM is capable of capturing bubble-swarm behaviour, its prediction error under GVF > 80% conditions still reaches approximately 20%. Yang et al. [13] identified gas accumulation on the suction side of the diffuser as the primary cause of efficiency degradation, but did not provide corresponding geometric-parameter control strategies. Meanwhile, advanced turbulence simulation methods, such as a continuous eddy simulation, have been proposed to improve modelling accuracy at high Reynolds numbers with reduced computational cost [14]. In addition, systematic assessments of Reynolds-Averaged Navier–Stokes (RANS) models have demonstrated that the SST k–ω model exhibits superior performance in predicting wall-bounded turbulent heat transfer and complex flow structures under wide Reynolds number ranges [15]. Furthermore, the presence of dissolved gases and phase-change phenomena can significantly influence flow stability and energy conversion processes. Previous studies on cavitating and gas–liquid flows have shown that dissolved gas concentration alters cavitation inception and development characteristics, thereby affecting discharge performance and flow stability [16]. These findings further highlight the complexity of multiphase transport mechanisms in turbomachinery systems.

With respect to structural parameter optimization, previous studies have reported diverse and sometimes conflicting conclusions. Ma et al. [17] demonstrated through systematic experiments that increasing the blade number from five to seven results in a 12% efficiency reduction. Xue et al. [18] proposed a spherical hub structure that reduces the separation region by 35%, yet such studies are largely based on trial-and-error approaches. Although the orthogonal experiments conducted by Li and Li [19,20] indicated that axial length has a significant influence on pump performance, parameter-interaction effects were not quantified. Han et al. [21,22] introduced trailing-edge flap designs for multiphase pump blades, achieving a 3.4% efficiency improvement when the flap length is 0.25 L_0 and the deflection angle is 5°, but this optimal configuration is only applicable under IGVF < 10% conditions. Liu [23] optimized a three-stage multiphase pump by controlling the velocity moment, reducing rotor–stator interference losses by 25%. However, experiments by Shi et al. [24,25] revealed that when the number of diffuser blades exceeds eight, pump efficiency decreases due to intensified secondary-flow effects. Overall, these structural

modifications lack quantitative sensitivity assessments, resulting in limited generality and reduced guidance value for design optimization.

Global sensitivity analysis (GSA) has emerged as a powerful tool for optimization in fluid machinery [26–29], among which the Sobol method and Morris screening method are the two most widely used approaches [30]. The Sobol method provides a benchmark framework for quantifying parameter-interaction effects, and the total sensitivity index developed by Saltelli et al. [30] accounts for both first-order effects and all higher-order interaction contributions. However, for models involving more than three structural parameters, Sobol analysis typically requires on the order of 10^4 simulations [31], leading to prohibitively high computational costs. In contrast, the Morris screening method can reduce computational demand by approximately 90% [32,33], but it is unable to capture nonlinear coupling effects. Feng et al. [26] proposed a coupled Morris–Sobol strategy that reduced the optimization cost of an aero-compressor by 70%, while Nabi et al. [34] further improved the robustness of the Morris–Sobol framework for skewed distributions through repeated sampling. Despite extensive research on multiphase pumps, the quantitative influence mechanisms of impeller geometric parameters on gas-phase transport capability under ultra-high GVF conditions (GVF > 80%) remain unclear. Current design methodologies still rely primarily on single-phase empirical correlations or experimental data obtained under low GVF conditions (<30%), resulting in several limitations: (1) a lack of systematic investigation into the combined effects of multiple geometric parameters on gas–liquid transport performance at high GVF levels [35]; (2) insufficient quantification of parameter-interaction mechanisms; and (3) unclear sensitivity ranking of key geometric parameters. These gaps motivate the present study to establish a quantitative sensitivity analysis framework for multiphase pumps operating under ultra-high GVF conditions.

Therefore, this study has two primary objectives:

(1) to establish the first sensitivity evaluation framework for impeller parameters under a GVF of 80% by integrating the Morris screening method for rapid identification of dominant parameters with Sobol global sensitivity analysis for accurate quantification of the interaction effects among impeller outer diameter (D), axial length (e), and blade wrap angle (θ); and (2) to propose a hierarchical impeller optimization strategy that aligns with engineering practice, enabling efficient parameter adjustment while reducing computational and design costs.

To achieve these objectives, a combined Python-based numerical simulation approach is adopted. First, theoretical analysis is used to guide the parameter design of the multiphase pump. A Plackett–Burman design is then employed to identify nine key structural parameters that significantly influence the external performance of the pump, including impeller outer diameter (D_0), axial length (L_s), blade wrap angle (φ), shroud inlet blade angle ($\beta_1 s$), hub inlet blade angle ($\beta_1 h$), blade number (Z), tip clearance (δ), hub half-cone angle (αh), and hub ratio (ν). For each parameter, seven variation levels are considered. All parameter combinations are simulated numerically, and the corresponding external performance data are recorded to construct a database.

Subsequently, the Morris method is applied to screen and rank the dominant parameters, followed by Sobol global sensitivity analysis to further quantify their contributions to pressure rise and parameter interaction effects. Finally, internal flow characteristics are compared across different configurations to clarify the physical influence of key parameters and to validate the sensitivity analysis results. All sensitivity calculations are implemented using Python2021, and the overall workflow is illustrated in Figure 1.

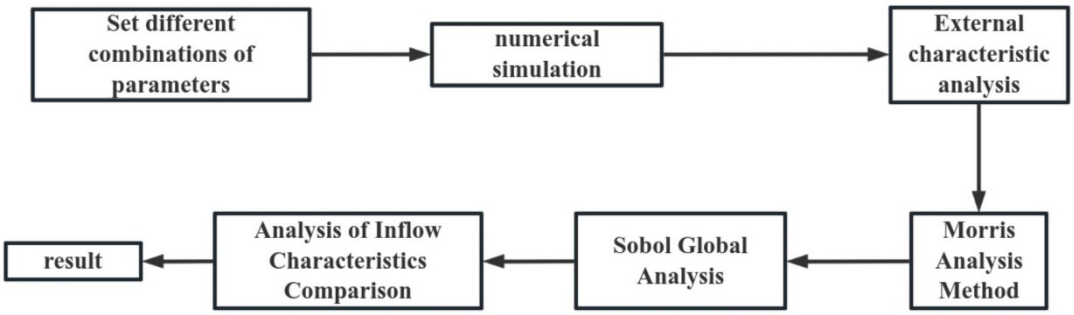
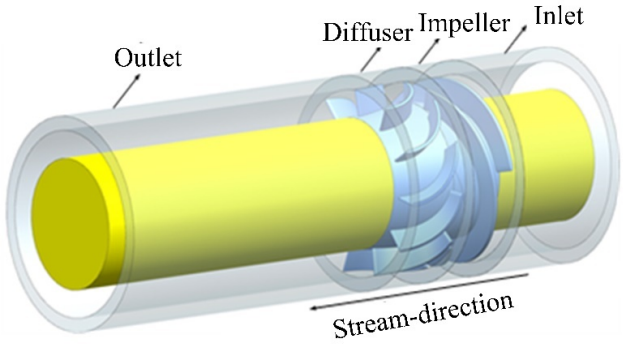


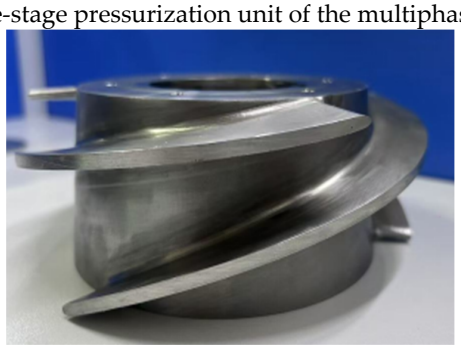
Figure 1. Flow chart of sensitivity analysis.

2. Research Object

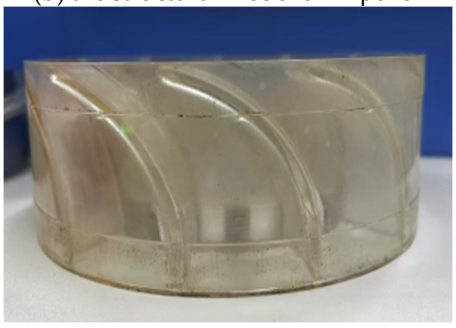
A multiphase pump with a design flow rate of 80 m^3/h is selected as the research object in this study. The key structural parameters of the multiphase pump are summarized in Table 1. The main components of the pressurization unit are illustrated in Figure 2, where Figure 2a shows the single-stage pressurization unit of the multiphase pump, Figure 2b shows the structural model of the impeller, and Figure 2c shows the structural model of the diffuser. The overall meridional geometry is presented in Figure 3. The pump mainly consists of inlet and outlet extension sections, an impeller, and a diffuser.



(**a**) Single-stage pressurization unit of the multiphase pump.



(**b**) the structural model of Impeller



(**c**) the structural model of Diffuser

Figure 2. Geometric model of the multiphase pump.

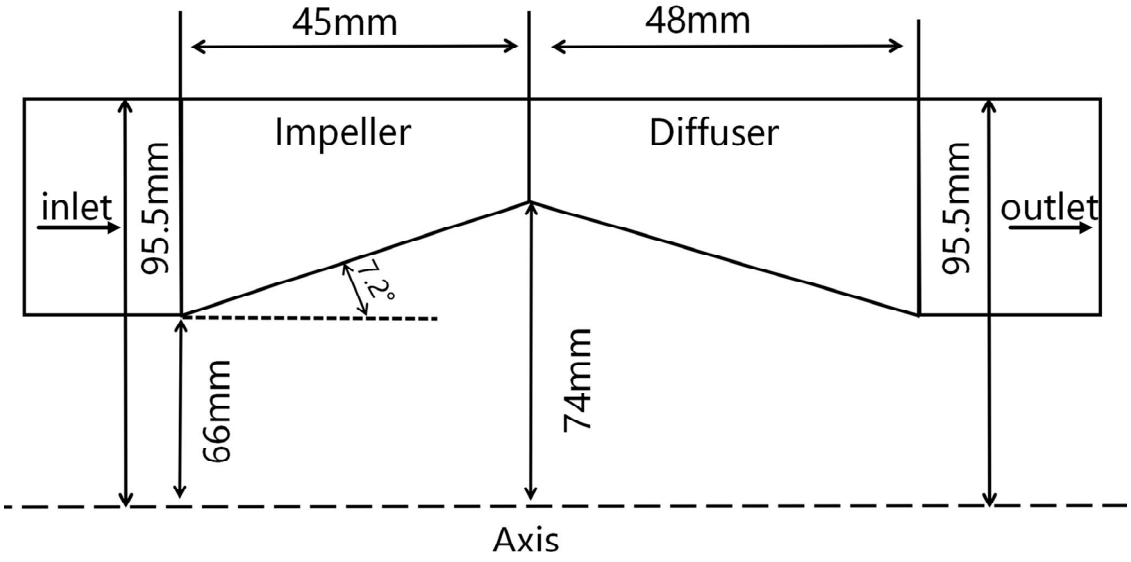


Figure 3. Meridional plane of multiphase pump.

Table 1. Key structural parameters of the multiphase pump.

	Symbol	Unit	Value
Diameter of the impeller	D_1	mm	191
Number of impeller blades	Z_1		6
Number of diffuser blades	Z_2		17
Cornerite of Impeller	θ	°	120
Axial length of impeller	e	mm	50
Hub ratio	d		0.7
Design flow	Q	m^3/h	80
Design speed	N	r/min	4500

3. Research Strategy

Based on the design conditions of the multiphase pump with a flow rate of 80 m^3/h, the external performance characteristics are first evaluated. As described above, the impeller is the core component governing the multiphase transport performance of the pump. The objective of this study is to investigate the effects of nine key impeller geometric parameters—particularly the impeller outer diameter, axial length, and blade wrap angle—on multiphase pump performance.

Starting from the baseline impeller configuration, only the impeller outer diameter, axial length, and blade wrap angle are varied, while other structural parameters, including blade number, hub ratio, blade solidity, and inlet/outlet blade setting angles, are kept constant to ensure fair comparison. To standardize parameter variations, a dimensionless parameter ($a = \text{Variable}/\text{Variable}_0$) is introduced to represent the relative deviation from the design value. Seven levels of the dimensionless parameter are considered, namely 0.91, 0.94, 0.97, 1.00, 1.03, 1.06, and 1.09. In total, nine structural parameters are examined, resulting in 63 computational cases. The detailed combinations of geometric parameters are listed in Table 2.

For all cases, geometric modeling, mesh generation, and numerical simulations are performed, followed by post-processing analysis of the simulation results. By comparing the external performance and internal flow characteristics among different configurations, the effects of impeller geometric parameter variations on gas–liquid two-phase flow behavior are systematically investigated. The resulting data are further subjected to sensitivity

analysis to identify the structural parameters that exert the greatest influence on multiphase pump performance and to summarize the corresponding governing trends.

Table 2. Parameter combinations of different design variables for the multiphase pump.

Variable	Design	Variable 1	Variable 2	...	Variable 63
Diameter of the impeller	191 mm	168 mm	173.8 mm	...	191 mm
Cornerite of impeller	120°	105°	120°	...	109.2°
Axial length of impeller	50 mm	44 mm	50 mm	...	50 mm
Number of impeller blades	6	6	7	...	8
Hub half cone angle	9.1°	9.1°	9.1°	...	9.6°
Inlet setting angle	5.6°	5.6°	5.6°	...	6.1°
	0.1 mm	0.2 mm	0.3 mm		0.4 mm
Hub half cone angle	7.5°	7.5°	7.5°	...	8.0°
Hub ratio of impeller	0.7	0.7	0.7	...	0.66

4. Mesh Generation

Unstructured meshes with strong adaptability are adopted for the inlet and outlet chambers, while structured meshes for the impeller and diffuser are generated using Turbogrid2021, as shown in Figure 4. In addition, refined boundary-layer meshes with an O-topology are applied near the walls of the impeller and diffuser to accurately resolve near-wall flow behavior. Specifically, Figure 4a presents the impeller mesh, whereas Figure 4b presents the diffuser mesh. To quantify the numerical uncertainty associated with spatial discretization, a grid-independence study is performed using four successively refined mesh levels (Case I–Case IV). The total cell count refers to the total number of cells in the entire computational domain, obtained by summing the inlet chamber, impeller, diffuser, and outlet chamber meshes. The pressure rise under the design operating condition is selected as the primary monitored quantity for grid-convergence assessment, while efficiency is used as a supplementary indicator.

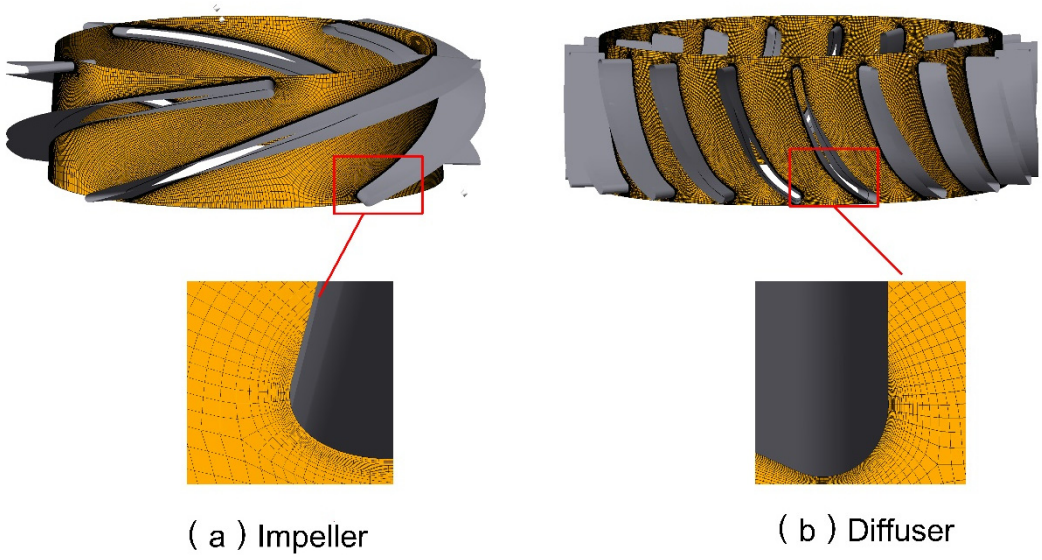


Figure 4. Mesh distribution of the impeller and diffuser flow passages.

For clarity, the normalized pressure rise is defined as

$$\Delta p^* = \frac{\Delta p_i}{\Delta p_{CaseI}} \quad (1)$$

where Δp_i is the predicted pressure rise at mesh level iii, and Δp_{CaseI} is the pressure rise predicted on the coarsest mesh.

The deviation relative to the finest mesh is defined as

$$\varepsilon_i = \left| \frac{\Delta p_i - \Delta p_{CaseIV}}{\Delta p_{CaseIV}} \right| \times 100\% \quad (2)$$

where Δp_{CaseIV} is the pressure rise predicted on the finest mesh.

As shown in Table 3, the predicted pressure rise exhibits a monotonic convergence trend as the mesh is refined. The deviation relative to the finest mesh decreases from 4.76% (Case I) to 2.38% (Case II) and further to 0.79% (Case III). The efficiency also shows monotonic convergence from 43.0% to 46.6%. When the total number of cells exceeds 17.66 million (Case III), further refinement to 22.36 million cells (Case IV) results in only a minor change in global performance, indicating that the numerical solution is essentially grid-independent. Therefore, Case III is selected for all subsequent simulations as a compromise between numerical accuracy and computational cost.

Table 3. Grid quality and grid-convergence information for the computational domain.

Mesh Level	Case I	Case II	Case III	Case IV
Inlet ($\times 10^4$)	305	424	514	641
Impeller ($\times 10^4$)	315	402	511	635
Diffuser ($\times 10^4$)	142	237	326	442
Outlet ($\times 10^4$)	212	305	415	518
Total (million)	9.74	13.68	17.66	22.36
Normalized head H	1.000	1.022	1.035	1.038
Deviation ε_i	3.66%	1.54%	0.29%	0
Efficiency (%)	42.7	43.2	43.8	43.9
Min orthogonality	0.12	0.13	0.13	0.14
Max aspect ratio	300	300	300	300
Wall y^+	1.03	1.05	1.06	1.06
Inflation layers	5	5	5	5

To further comply with best-practice recommendations, a grid convergence index (GCI) analysis based on Richardson extrapolation is conducted using three consecutively refined meshes (Case II–Case IV). The observed order of convergence for pressure rise is p = 7.470, the Richardson-extrapolated pressure rise is 0.12725 MPa, and the fine-grid GCI is 1.24%. For efficiency, the corresponding fine-grid GCI is 0.65%. These results indicate that the numerical uncertainty associated with grid resolution is acceptable for the present sensitivity analysis study.

In addition, the adopted mesh satisfies the near-wall resolution requirement of the SST turbulence model. The minimum mesh orthogonality is 0.12, the maximum aspect ratio is 300, five inflation layers are applied, and the dimensionless wall distance is maintained at approximately $y^+ \approx 1.03$.

5. Mathematical and Numerical Modelling of Gas–Liquid Two-Phase Flow

5.1. Governing Equations

In the present study, the gas–liquid two-phase flow inside the multiphase pump is modelled using an Euler–Euler two-fluid approach, in which both phases are treated as interpenetrating and continuous media. This formulation is particularly suitable for high gas volume fraction (GVF) conditions, where strong interphase coupling and phase interactions dominate the flow behaviour. For each phase k ($k = g$ for gas and $k = l$

for liquid), the governing equations consist of a continuity equation and a momentum equation. The continuity equation is written as

$$\frac{\partial(\alpha_k \rho_k)}{\partial t} + \nabla \cdot (\alpha_k \rho_k u_k) = 0 \tag{3}$$

where α_k, ρ_k, and u_k denote the volume fraction, density, and velocity vector of phase, respectively.

The momentum conservation equation for phase k is expressed as

$$\frac{\partial(\alpha_k \rho_k u_k)}{\partial t} + \nabla \cdot (\alpha_k \rho_k u_k u_k) = -\alpha_k \nabla p + \nabla \cdot (\alpha_k \tau_k) + \alpha_k \rho_k g + M_k \tag{4}$$

where p is the shared pressure field, τ_k is the viscous stress tensor of phase k, g is the gravitational acceleration, and M_k represents the interphase momentum transfer term.

The volume fractions of the two phases satisfy the constraint

$$\alpha_g + \alpha_l = 1 \tag{5}$$

5.2. Interphase Momentum Transfer Models

The interphase momentum transfer term M_k accounts for the dominant interaction forces between the gas and liquid phases. Under high GVF conditions, the primary interphase forces include drag force, virtual mass force, lift force, and turbulent dispersion force. Accordingly, the total interphase force acting on phase k can be expressed as

$$F_{M,k} = F_{D,k} + F_{A,k} + F_{L,k} + F_{T,k} \tag{6}$$

The drag force is modelled as

$$F_{D,k} = \frac{3}{4} C_D \frac{\alpha_g \alpha_l \rho_l}{d_b} |u_g - u_l| (u_g - u_l) \tag{7}$$

where C_D is the drag coefficient and d_b is the characteristic bubble diameter.

The virtual mass force is given by

$$F_{vm} = C_m a_g \rho_l \left(\frac{Du_l}{Dt} - \frac{Du_g}{Dt} \right) \tag{8}$$

where C_{VM} is the virtual mass coefficient.

The lift force is expressed as

$$F_{L,k} = C_L \rho_l \alpha_g (u_g - u_l) \times (\nabla \times u_l) \tag{9}$$

and the turbulent dispersion force is modelled as

$$F_{T,k} = -C_T \rho_l \nabla (\alpha_g k_l) \tag{10}$$

where k_l is the turbulent kinetic energy of the liquid phase.

In the present study, the drag coefficient, virtual mass coefficient, lift coefficient, and turbulent dispersion coefficient are set to 0.44, 0.5, 0.5, and 0.1, respectively, following commonly adopted values in multiphase pump simulations. The Basset history force and Magnus force are neglected, as their contributions are generally small under high GVF and steady operating conditions.

5.3. Turbulence Modelling

Turbulence effects are modelled using a phase-dependent approach to account for the distinct turbulence characteristics of the continuous and dispersed phases.

For the liquid phase, the shear stress transport (SST) $k-\omega$ turbulence model is employed due to its proven capability in accurately predicting adverse pressure gradients, flow separation, and secondary flow structures in turbomachinery applications. To further improve the resolution of vortex-dominated flow features under high GVF conditions, an adaptive vortex-driven (AVD) correction is incorporated into the SST framework. This correction modifies the eddy viscosity in regions of strong rotational motion, enabling enhanced prediction of coherent vortical structures without introducing excessive numerical dissipation.

For the gas phase, a zero-equation turbulence model is adopted. Under high GVF conditions, the gas phase behaves as a dispersed medium with limited turbulence self-generation, and its turbulent characteristics are primarily governed by the surrounding liquid-phase turbulence. The zero-equation model therefore provides a reasonable balance between physical fidelity and numerical robustness.

5.4. Near-Wall Treatment and Mesh Requirements

An automatic wall treatment based on the $k-\omega$ formulation is applied at all solid boundaries. This approach allows a smooth transition between wall-function treatment and low-Reynolds-number resolution, depending on the local grid resolution. To satisfy the near-wall resolution requirements of the SST $k-\omega$ model, boundary-layer meshes with O-topology are generated along the blade, hub, and shroud surfaces. The mesh is refined to ensure that the dimensionless wall distance y^+ remains below unity over most wall-adjacent regions, thereby ensuring accurate prediction of near-wall flow behaviour.

6. Numerical Setup and Boundary Conditions

6.1. Numerical Solver and Discretization

All numerical simulations are performed using ANSYS CFX2021. Water and air are selected as the liquid and gas phases, respectively. The liquid phase is treated as the continuous phase, while the gas phase is treated as the dispersed phase. The governing equations are solved using a finite-volume method. First-order upwind discretization schemes are employed for the convection terms and turbulent quantities to enhance numerical stability under high gas volume fraction conditions. Although first-order schemes may introduce numerical diffusion, this effect is mitigated by the use of a sufficiently refined mesh, as confirmed by the grid independence study.

Convergence is assessed based on the root-mean-square (RMS) residuals of all governing equations, with a convergence criterion of 1×10^{-5}.

6.2. Rotor–Stator Interface and Steady-State Assumption

The interaction between the rotating impeller and stationary diffuser is modelled using the Frozen Rotor approach. This steady-state multiple-reference-frame method captures the circumferentially averaged interaction between rotor and stator components and provides stable and computationally efficient solutions.

The Frozen Rotor approach is adopted in the present study to reduce the computational cost associated with the large number of parametric simulations required for sensitivity analysis. Although transient simulations can provide more detailed unsteady flow features, previous studies have demonstrated that the Frozen Rotor method is sufficient for accurately predicting the time-averaged performance indicators, such as pressure rise and efficiency, which are the primary focus of this work. Moreover, the Sobol-based

global sensitivity analysis requires on the order of 10^4 simulations for statistical convergence; performing fully transient calculations for each case would increase the computational cost by at least an order of magnitude, rendering the parametric study impractical. Therefore, modelling the gas phase as an ideal gas and adopting steady-state Frozen Rotor simulations together provide a reasonable balance between physical fidelity and computational efficiency.

6.3. Boundary Conditions and Fluid Properties

A mass-flow inlet boundary condition is imposed at the pump inlet, corresponding to the design flow rate of $Q = 80\ \mathrm{m}^3/\mathrm{h}$. The inlet gas and liquid volume fractions are specified as 0.8 and 0.2, respectively, to represent high GVF operating conditions. A static pressure outlet boundary condition is applied at the pump outlet. No-slip boundary conditions are imposed on all solid walls. The impeller rotational speed is fixed at 4500 r/min.

The physical properties of the working fluids are set as follows: the density and dynamic viscosity of the liquid phase (water) are $\rho_l = 998\ \mathrm{kg/m^3}$ and $u_l = 1.0 \times 10^{-3}\ \mathrm{Pa \cdot s}$, respectively, while the density and dynamic viscosity of air are $p_g = 1.225\ \mathrm{kg/m^3}$ and $u_g = 1.8 \times 10^{-5}\ \mathrm{Pa \cdot s}$.

The working fluids are water and air. The liquid phase is treated as an incompressible Newtonian fluid, while the gas phase is modelled as an ideal gas. The density and dynamic viscosity of water at 20 °C are specified as $998\ \mathrm{kg/m^3}$ and $1.002 \times 10^{-3}\ \mathrm{Pa \cdot s}$, respectively. The dynamic viscosity of air at 20 °C and 1 atm is specified as $1.82 \times 10^{-3}\ \mathrm{Pa \cdot s}$. The gas density is calculated using the ideal-gas equation of state within the solver to account for compressibility effects under high gas volume fraction conditions. Temperature variation and its influence on fluid properties are neglected because the present study focuses on geometric-parameter sensitivity under approximately isothermal conditions.

6.4. Grid Independence Assessment

A grid-independence study is conducted to evaluate the numerical uncertainty associated with spatial discretization. Four mesh levels with increasing grid density are generated for the entire computational domain. As the total number of grid cells increases, the predicted pressure rise and efficiency exhibit monotonic convergence trends. When the total number of grid cells exceeds 17.66 million, the variation in predicted global performance remains small, indicating that further mesh refinement has a negligible influence on the numerical results. Therefore, the mesh configuration corresponding to Case III is selected as a compromise between numerical accuracy and computational efficiency for all subsequent simulations.

6.5. Sensitivity Analysis Methods

Sensitivity analysis is a systematic mathematical and engineering approach used to evaluate the dependence of response variables on variations in input parameters, thereby identifying key influencing factors, quantifying uncertainty, and supporting system optimization and decision-making. Common sensitivity analysis methods include the Sobol index method, the Morris screening method, and the FAST method. In the present study, the Morris screening method is first employed to rapidly identify dominant structural parameters, followed by Sobol global sensitivity analysis to accurately quantify their contributions to multiphase pump performance.

The Morris screening method is a qualitative global sensitivity analysis technique designed for the efficient identification of input parameters that have a significant impact on model outputs. Its core concept is to assess parameter sensitivity through directional perturbations, known as elementary effects (*EE*), making it particularly suitable for high-dimensional models. By performing multiple random samplings based on trajectory

designs, the method evaluates the mean effect (μ) and standard deviation (σ) of each parameter's influence on the output, thereby distinguishing linear effects from nonlinear or interaction effects. The elementary effect (EE) is defined as follows:

$$EE_i = \frac{f(X_1, \ldots, X_i + \Delta, \ldots, X_k) - f(X)}{\Delta} \tag{11}$$

where X denotes the input parameter vector and Δ represents the fixed step size.

Sensitivity indices:

Mean (μ): reflects the average effect of an input parameter on the model output.

$$\mu_i = \frac{1}{r}\sum_{j=1}^{r} EE_i^{(j)} \tag{12}$$

Standard deviation (σ): reflects the degree of nonlinearity or interaction effects of an input parameter on the model output.

$$\sigma_i = \sqrt{\frac{1}{r}\sum_{j=1}^{r}\left(EE_i^{(j)} - \mu_i\right)^2} \tag{13}$$

The Sobol sensitivity analysis method, also known as the variance-based method, decomposes the total variance of the model output into contributions from individual input parameters and their interaction effects. Sobol indices are evaluated using Monte Carlo integration, including the first-order index, which represents the main effect of an individual parameter, and the total-effect index, which accounts for both the parameter's independent contribution and all higher-order interaction effects. The corresponding formulations are given as follows:

The total variance (D) is defined as:

$$D = Var(Y) = \int f^2(X)dX - f_0^2 \tag{14}$$

where f_0 denotes the mean value of the model output.

First-order index (main effect, Si):

$$Si = \frac{VarX_i(EX_{\sim i}(Y|X_i))}{D} \tag{15}$$

It represents the proportion of output variance caused solely by the individual input parameter Xi.

Total-effect index (S_{Ti}):

$$S_{Ti} = 1 - \frac{Var_{X\sim i}(E_{Xi}(Y|X_{\sim i}))}{D} \tag{16}$$

The total-effect index (S_{Ti}) includes the contribution of Xi and all its interaction effects with other input parameters.

Numerical simulations are performed using ANSYS CFX2021, with air and liquid water selected as the transport media to investigate the effects of gas volume fraction and flow rate on multiphase pump performance. The two-phase system consists of water as the continuous phase and air as the dispersed phase. The SST turbulence model is applied to the liquid phase, while a zero-equation turbulence model is used for the gas phase. The operating flow rate is set to Q = 80 m^3/h, and the impeller rotational speed is fixed at 4500 r/min. A mass-flow inlet boundary condition is imposed, with the inlet mass flow determined according to the pump operating condition. The inlet gas and liquid volume

fractions are specified as 0.8 and 0.2, respectively. A pressure outlet boundary condition is applied at the outlet. Interfaces between stationary components are treated using the None option, while rotor–stator interfaces are modeled using the Frozen Rotor approach, which provides a stable solution for multiple reference frame problems. At the walls, an automatic wall treatment based on the $k - \omega$ formulation is adopted, allowing a smooth transition from wall functions to low-Reynolds-number formulations in the near-wall region. First-order upwind schemes are used for the convection terms and turbulent quantities, and the convergence criterion is set to an RMS residual of 1×10^{-5}.

7. Experimental Validation

To ensure the accuracy and reliability of the numerical simulations, experimental tests were conducted under the operating conditions considered in this study. The experimental test rig mainly consists of the pump assembly (Figure 5), pressure sensors, an electromagnetic flowmeter, an air compressor, and control valves, as schematically illustrated in Figure 6. Different gas volume fraction (GVF) conditions were achieved by adjusting the air compressor pressure and the liquid flow rate. The pressure rise in the multiphase pump under various operating conditions was measured using pressure sensors installed at the inlet and outlet sections. The experimentally obtained external performance characteristics were then compared with the corresponding numerical predictions. Figures 7 and 8 present the comparison between numerical and experimental results, as well as photographs of the experimental setup. The numerical performance data were obtained by averaging the results of transient simulations after reaching statistically steady states. Within the operating range of 0.6–1.2 times the rated flow rate, the relative error between the numerical and experimental pressure rise remains below 2%, demonstrating good agreement between simulations and experiments and confirming the reliability of the adopted numerical methodology. In the performance comparison, error bars are included to represent both experimental and numerical uncertainties. The experimental error bars reflect the overall measurement uncertainty of the test system, whereas the numerical error bars are estimated using the grid convergence index (GCI) analysis. Based on the grid-convergence results, the numerical uncertainty is taken as 1.24% for pressure rise and 0.65% for efficiency.

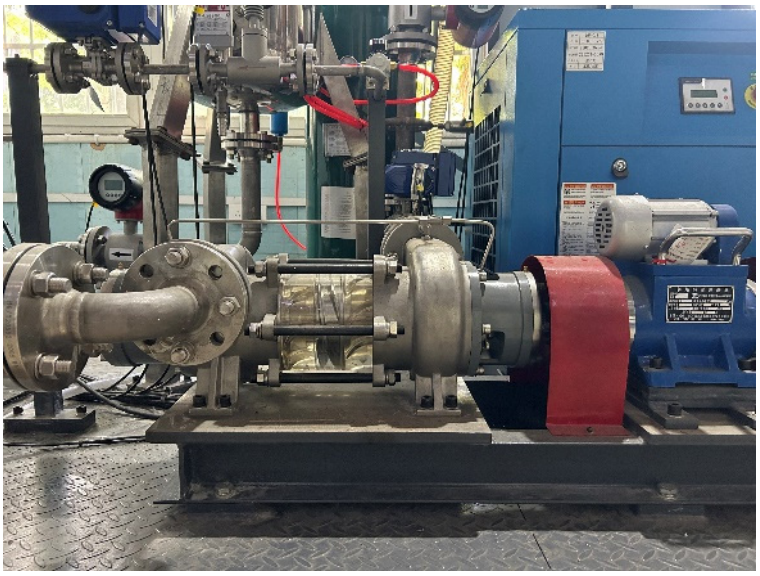


Figure 5. Physical view of the pump body in the experimental test bench.

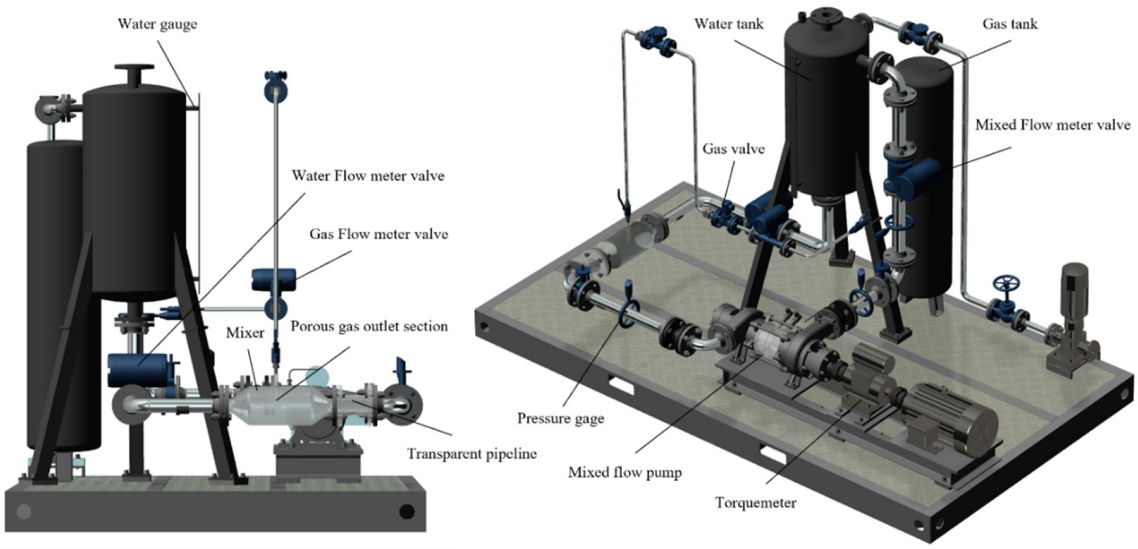


Figure 6. Overall layout of the experimental test bench.

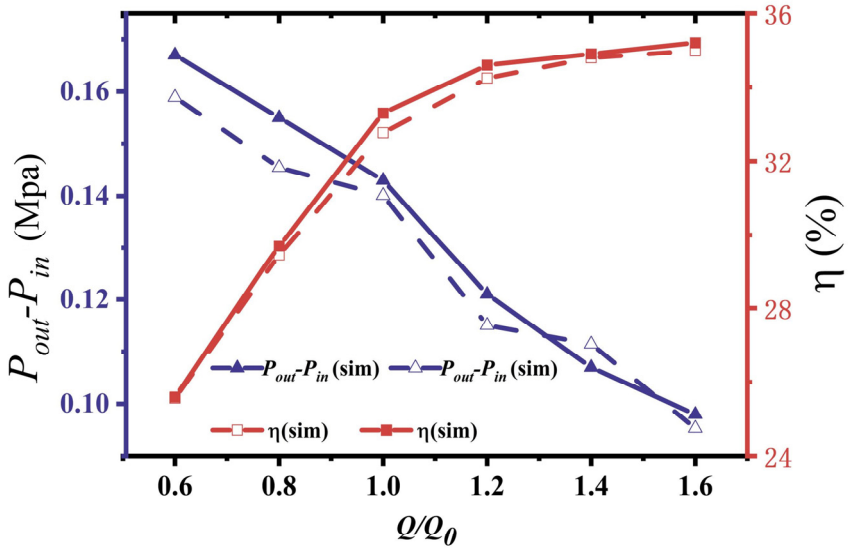


Figure 7. Comparison of experimental and numerical pressure rise and efficiency of the multiphase pump under different operating conditions, including experimental uncertainty bars and numerical uncertainty bars estimated from GCI analysis.

In addition to external performance measurements, flow visualization experiments were conducted to qualitatively examine the internal gas–liquid flow structures under different flow-rate conditions. Figure 8 shows the distribution of gas–liquid flow patterns inside the impeller passages at different normalized flow rates (Q/Q_0 = 0.6–1.4). At low flow rate (Q/Q_0 = 0.6), obvious gas accumulation and non-uniform phase distribution are observed in the blade passages, indicating intensified phase separation and local flow blockage. As the flow rate increases to Q/Q_0 = 0.8–1.0, the gas–liquid mixture becomes more uniformly distributed, and the interphase slip is significantly reduced, corresponding to the stable operating region of the pump. Under these conditions, the flow exhibits relatively smooth and coherent structures, which is consistent with the high efficiency and pressure-rise performance observed in both experiments and simulations.

When the flow rate further increases to Q/Q_0 = 1.2–1.4, strong shear effects and flow instabilities emerge. Large-scale gas clusters and intensified turbulent mixing are observed near the blade surfaces and passage outlets, indicating enhanced energy dissipation and deteriorated flow stability. These experimental observations are in good qualitative agreement

with the numerical predictions of internal flow structures and turbulent characteristics. The consistency between measured performance data, flow visualization results, and CFD simulations further validates the accuracy and robustness of the proposed numerical modelling framework.

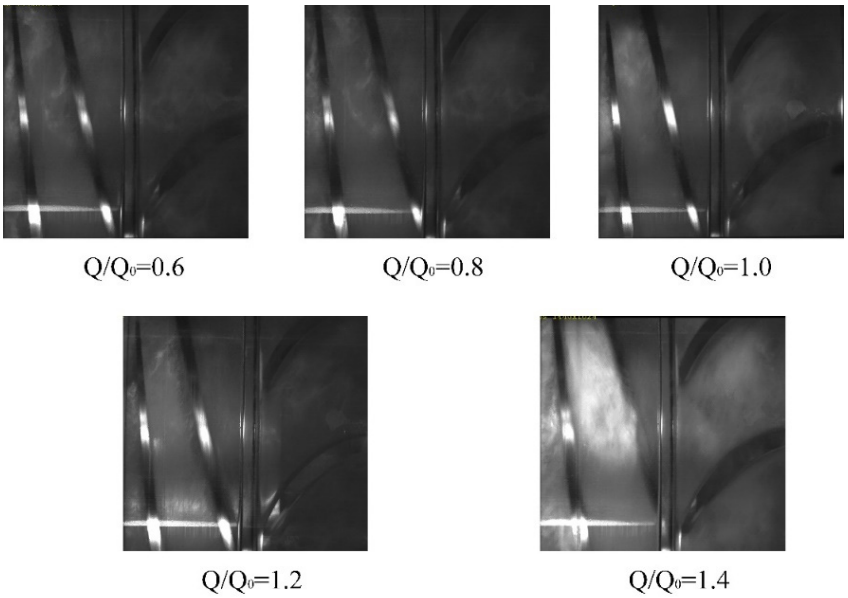


Figure 8. Photograph of the experimental test rig.

8. Results and Discussion

8.1. Effects of Key Structural Parameters on External Performance

Figures 9 and 10 present the bar charts illustrating the effects of the dimensionless values of nine key impeller geometric parameters on pump efficiency and pressure rise (Pout-Pin), respectively. The results indicate that both efficiency and pressure rise exhibit pronounced nonlinear responses to parameter variations within the range of 0.91–1.09. For most parameters, either efficiency or pressure rise reaches an extremum at the dimensionless value of 1.00 (the baseline design), suggesting that this value represents a critical balance point.

With respect to the impeller outer diameter, increasing the dimensionless value from 0.91 to 1.00 results in a decrease in efficiency from 34.6% to 32.55%, while the pressure rise increases from 0.122 Mpa to 0.143 Mpa. Further increasing the diameter to 1.09 leads to a slight recovery in efficiency (28.9%) but a reduction in pressure rise to 0.122 Mpa, indicating that moderate enlargement of the outer diameter enhances pressurization, whereas excessive enlargement weakens this effect. For axial length, efficiency decreases monotonically from 33.92% to 27.9% as the dimensionless value increases from 0.91 to 1.09. The pressure rise peaks at 0.143 Mpa near the design point and subsequently declines, implying the existence of an optimal axial length range, beyond which pressurization performance deteriorates.

The blade wrap angle shows a strong positive correlation with efficiency, which increases from 25.9% to 35.7% as the dimensionless value increases from 0.91 to 1.09. In contrast, the pressure rise reaches a maximum of 0.143 Mpa at the design value and then decreases with further increases in wrap angle, owing to enhanced flow separation and vortex-induced losses at excessive wrap angles. The shroud inlet blade angle has a minor influence on efficiency (32.3–32.55%), but the pressure rise decreases from 0.152 Mpa to 0.135 Mpa as the angle increases, mainly due to intensified impact losses.

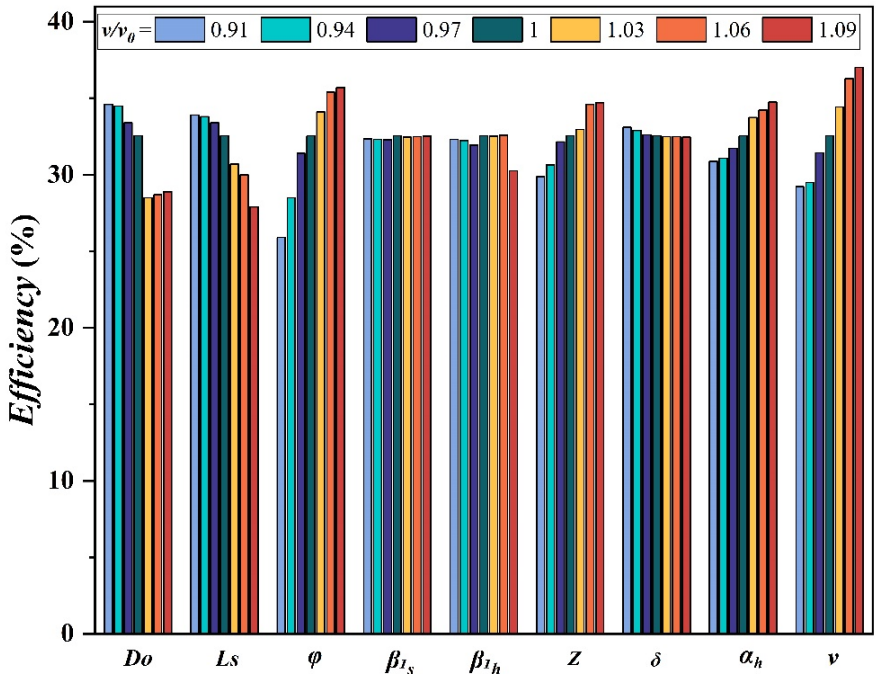


Figure 9. Bar charts of efficiency performance of the multiphase pump under different structural parameters.

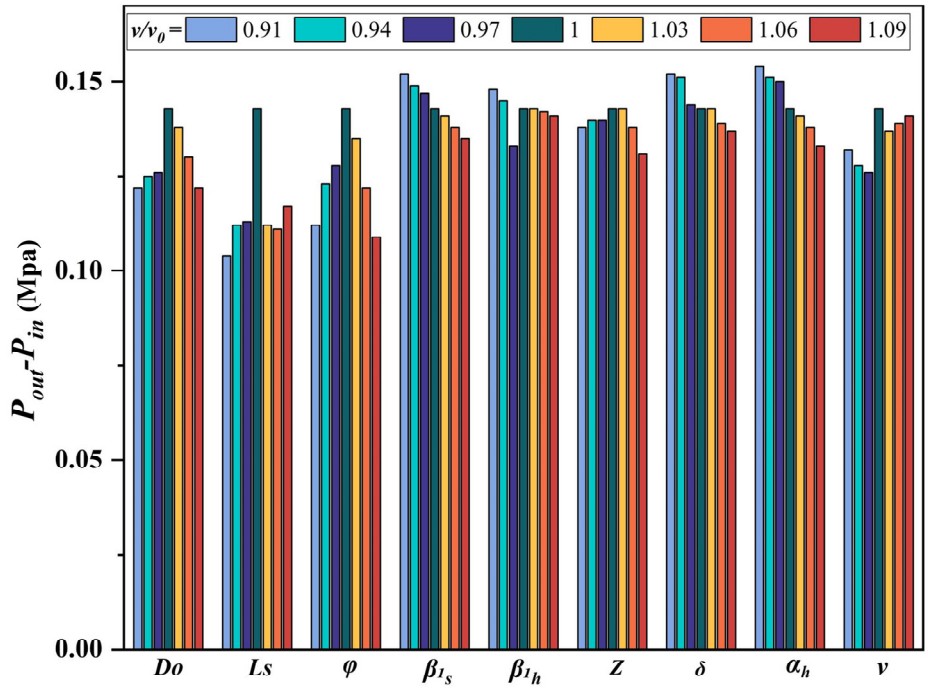


Figure 10. Bar charts of pressure-rise performance of the multiphase pump under different structural parameters.

For the hub inlet blade angle, efficiency reaches a local maximum of 32.58% at a dimensionless value of 1.06 and then drops sharply to 30.25%, indicating the presence of an optimal configuration; excessive angles tend to cause partial blockage of the flow passage. A significant reduction in pressure rise is observed near 0.97, which is associated with changes in the hub passage geometry. Increasing the blade number from 0.91 to 1.09 enhances efficiency from 29.88% to 34.72%, while the pressure rise peaks at approximately 0.143 Mpa within the range of 1.00–1.03 and then decreases due to increased friction losses caused by overly dense blade arrangements.

The tip clearance exhibits a weak negative correlation with efficiency (from 33.1% to 32.45%), whereas the pressure rise decreases markedly from 0.152 Mpa to 0.137 Mpa as the clearance increases, primarily due to intensified leakage losses. For the hub half-cone angle, efficiency increases from 30.88% to 34.75% as the dimensionless value increases from 0.91 to 1.09, attributed to improved flow diffusion and reduced separation. However, the pressure rise continuously decreases, since excessive cone angles induce rapid passage expansion and low-pressure vortex formation. The hub ratio shows a strong positive correlation with efficiency (29.22–37.02%), while the pressure rise reaches a maximum at the design value and then fluctuates slightly with further increases, reflecting the combined influence of passage geometry.

Overall, blade wrap angle, blade number, hub ratio, and hub half-cone angle have a significant impact on efficiency, which can be enhanced by increasing these parameters within appropriate ranges, although critical thresholds must be considered for wrap angle and blade number. In contrast, tip clearance and axial length are negatively correlated with efficiency and should be minimized or carefully constrained in design. From the perspective of pressure rise, impeller outer diameter, axial length, wrap angle, and hub ratio reach their optimal values near the baseline design, whereas the shroud inlet blade angle and hub half-cone angle exhibit negative correlations.

Based on cross-comparison of all cases, the maximum efficiency of 37.6% is achieved for the parameter combination D_0 = 186 mm, Ls = 50 mm, $\varphi = 140^\circ$, $\beta_1 s = 5.6^\circ$, $\beta_1 h = 7.5^\circ$, Z = 6, δ = 0.3, $\alpha h = 7.5^\circ$, and ν = 0.7. The maximum pressure rise of 0.154 Mpa is obtained for a similar configuration with D_0 = 191 mm, Ls = 56 mm, and $\varphi = 140^\circ$.

It should be noted that under practical operating conditions, these structural parameters do not influence external performance independently but exhibit strong coupling and interaction effects. The above external performance analysis only reflects the individual influence of each parameter and cannot fully capture their combined effects. Therefore, a Morris sensitivity analysis is further required to systematically screen and rank the relative importance of different structural parameters, which is addressed in the following section.

In the Morris sensitivity analysis, the mean effect reflects the overall directional influence of a structural parameter on the response, the absolute effect represents the overall magnitude of its influence regardless of direction, and the standard deviation indicates the degree of nonlinearity and interaction with other parameters. Based on the above Morris sensitivity analysis, the impeller outer diameter D_0, axial length Ls, and blade wrap angle φ are identified as the three dominant structural parameters affecting the performance of the multiphase pump. These parameters consistently exhibit the highest sensitivity levels in both efficiency and pressure-rise responses. In both Figures 11 and 12, the dashed lines denote the average values of all structural parameters for each sensitivity index. However, the Morris method mainly provides qualitative screening results and cannot quantitatively evaluate the relative contributions of individual parameters or their interaction effects. Therefore, Sobol global sensitivity analysis is further conducted to quantify the individual and coupled effects of these three dominant parameters. Considering the high computational cost of Sobol analysis, only these key geometric variables are selected for further investigation. To improve the accuracy and reliability of the Sobol analysis, additional samples are generated by increasing the sampling density and narrowing the parameter intervals of the impeller outer diameter, axial length, and blade wrap angle. The final variation ranges are set to 163–211 mm for the impeller outer diameter, 40–64 mm for the axial length, and 108–132° for the blade wrap angle. Numerical simulations are then performed for all sampled configurations, and the corresponding external performance data are collected for subsequent sensitivity analysis.

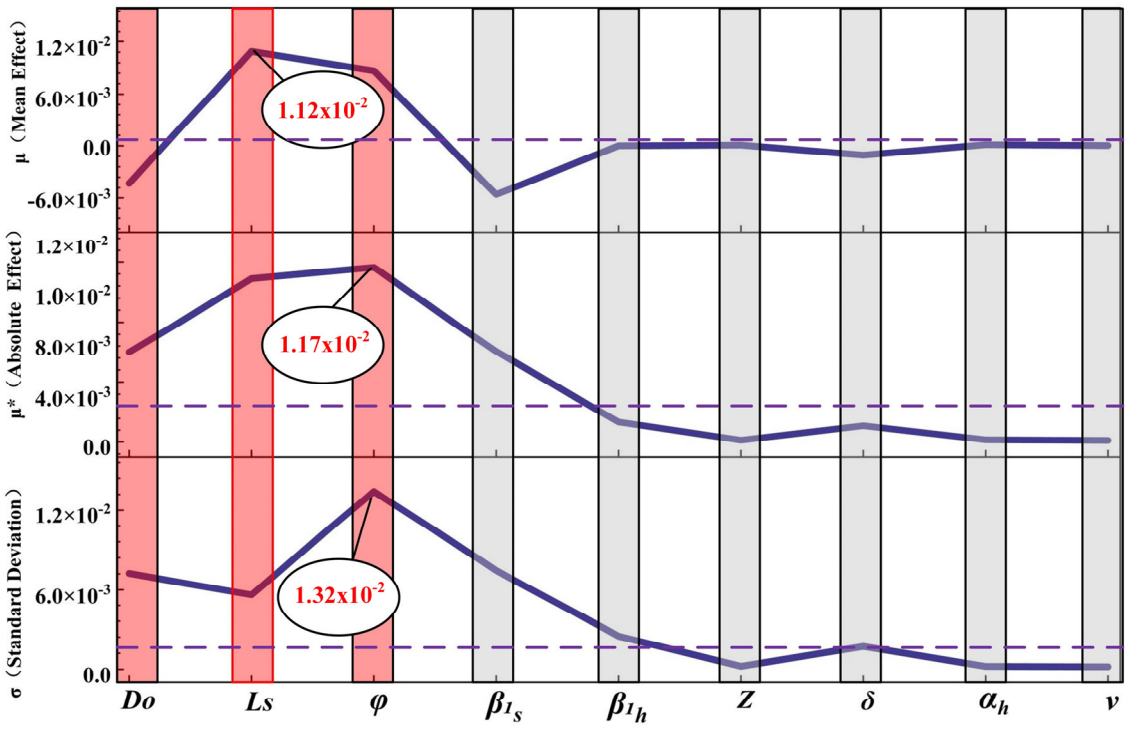


Figure 11. Efficiency response curves obtained from Morris sensitivity analysis.

Figure 11 presents the Morris sensitivity results for efficiency. Among all parameters, the axial length shows the largest mean effect, reaching 1.12×10^{-2}, whereas the blade wrap angle exhibits the largest absolute effect and standard deviation, with values of 1.17×10^{-2} and 1.32×10^{-2}, respectively. These results indicate that the effect of blade wrap angle on efficiency is not only strong but also highly nonlinear, with pronounced interaction effects. In contrast, most of the remaining structural parameters are below the average level indicated by the dashed lines, suggesting relatively weak influences on efficiency. This further implies that efficiency variation cannot be fully explained by the independent change of a single parameter, but is instead governed by coupled geometric effects. Secondary parameters, such as hub inclination, blade thickness, and clearance, exhibit relatively small mean effects and standard deviations, demonstrating limited influence under the investigated operating conditions.

A similar sensitivity pattern is observed for pressure rise, as shown in Figure 12. The blade wrap angle has the largest mean effect, with a value of 1.33×10^{-2}, and it also exhibits the largest absolute effect and standard deviation, reaching 1.64×10^{-2} and 1.31×10^{-2}, respectively. This confirms that the blade wrap angle plays a leading role in determining pressure-rise performance and is also involved in strong nonlinear and interaction effects. The impeller outer diameter and axial length also show considerable sensitivity, reflecting their important roles in flow development, residence time, and blade loading distribution. In addition, most of the remaining structural parameters are above the average level indicated by the dashed lines, indicating that pressure rise is generally more sensitive to geometric variations than efficiency. Compared with the efficiency response in Figure 11, the pressure-rise response in Figure 12 appears smoother, suggesting that pressure performance is more strongly governed by geometric scaling effects, whereas efficiency is more susceptible to complex coupling mechanisms, especially under ultra-high gas volume fraction conditions where phase separation and secondary flows become more significant.

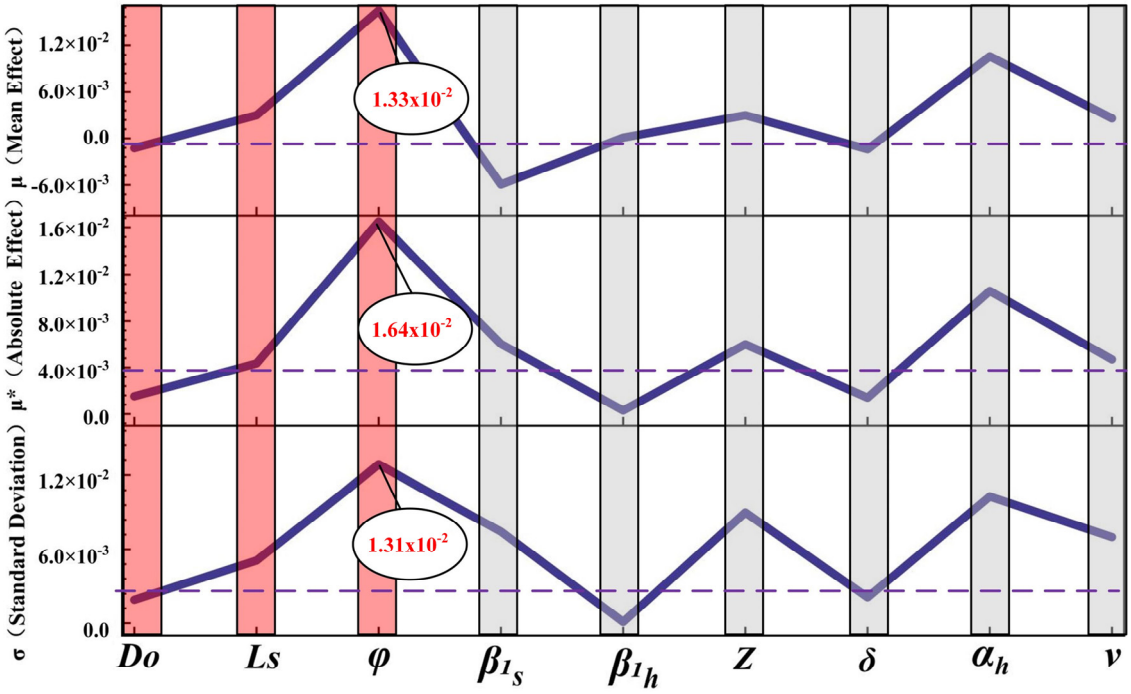


Figure 12. Pressure-rise response curves obtained from Morris sensitivity analysis.

Figure 13 presents the combined heat maps of pressure rise and efficiency for the three dominant structural parameters of the multiphase pump impeller, namely the impeller outer diameter, axial length, and blade wrap angle. The left side of the Figure 13 shows the pressure-rise heat maps, and the right side shows the corresponding efficiency heat maps. In each sub-map, two parameters vary simultaneously while the third parameter is fixed at its baseline design value. Darker color intensity indicates a higher pressure rise or efficiency under the corresponding parameter combination. The pressure-rise heat maps show that the parameter combinations with relatively high pressurization performance are mainly concentrated near the baseline design region. When one parameter is fixed at its design value, the combinations around the design values of the other two parameters generally exhibit darker colors, indicating stronger pressurization capability. This result suggests that pressure rise is sensitive to the coordinated variation in impeller outer diameter, axial length, and blade wrap angle.

In contrast, the efficiency heat maps show a broader and less concentrated distribution of favorable parameter combinations. Compared with the pressure-rise maps, the efficiency maps present a more complex response pattern, indicating that efficiency is affected by parameter variation in a less localized manner. In other words, relatively high efficiency can be achieved in a wider parameter range, whereas high pressure rise is concentrated in a narrower combination region.

Therefore, the combined heat-map results indicate that the dominant structural parameters affect pressure rise and efficiency in different ways. The pressure-rise performance is more concentrated around specific parameter combinations, while the efficiency response exhibits a broader and more irregular distribution. This difference further implies that the performance optimization of the multiphase pump should consider the coupling effects among structural parameters rather than relying only on single-parameter analysis.

To further investigate parameter interaction effects, Sobol global sensitivity analysis is employed to quantitatively evaluate the influence of individual parameters and their interactions on pressure rise and efficiency through the accurate calculation of first-order and total-effect indices.

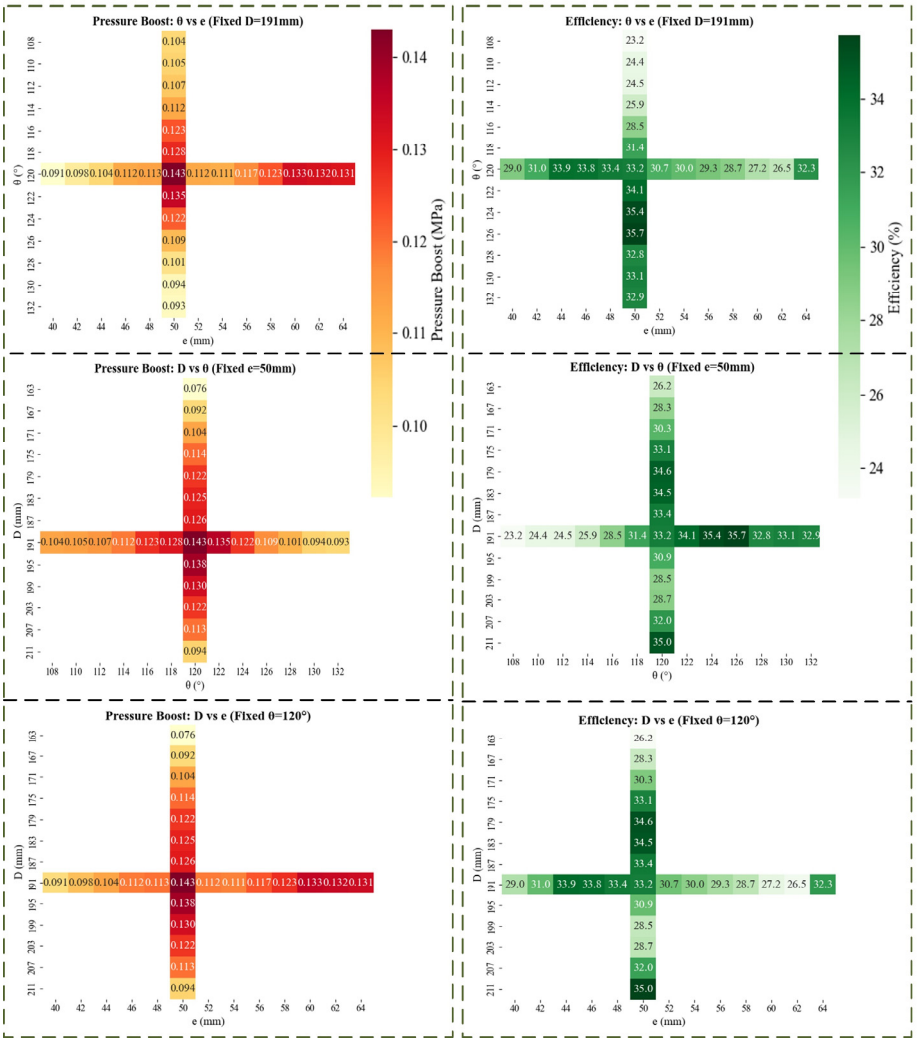


Figure 13. Heat maps of the external performance of the multiphase pump corresponding to different structural parameters based on Sobol sensitivity analysis.

Figure 14 presents the sensitivity analysis results for the three dominant impeller parameters—outer diameter, axial length, and blade wrap angle—on pressure rise and efficiency, including both first-order (main-effect) and total-effect indices. The first-order Sobol index (*Si*) represents the proportion of output variance explained solely by an individual parameter, reflecting its independent contribution. A value of Si close to unity indicates a strong individual influence, whereas a value close to zero implies a negligible independent effect. The total-effect index (S_{Ti}) accounts for the combined contribution of a parameter and all of its interaction effects with other parameters. The difference between Sti and Si therefore quantifies the strength of parameter interactions; when $S_{Ti} > Si$, joint optimization with other parameters becomes necessary, as adjusting the parameter alone has limited impact.

For pressure-rise performance, the impeller outer diameter exhibits the strongest independent influence, with a first-order index of $Si = 0.37$. Its total-effect index ($S_{Ti} = 0.47$) indicates the presence of interaction effects, although their contribution remains moderate. This result further confirms that the impeller outer diameter is the most critical parameter governing pressurization performance. The axial length shows the second-largest influence ($Si = 0.22$, $S_{Ti} = 0.33$), characterized by a moderate independent effect and relatively weak interactions. Although the blade wrap angle has a first-order index comparable to that of axial length ($Si = 0.25$), its considerably higher total-effect index ($S_{Ti} = 0.39$) suggests

that it influences pressure rise predominantly through synergistic interactions with other parameters. Overall, the total-effect indices of all three parameters are significantly higher than their corresponding first-order indices, indicating that parameter coupling plays an important role in determining pressure-rise performance, with the interaction effects involving blade wrap angle being particularly pronounced.

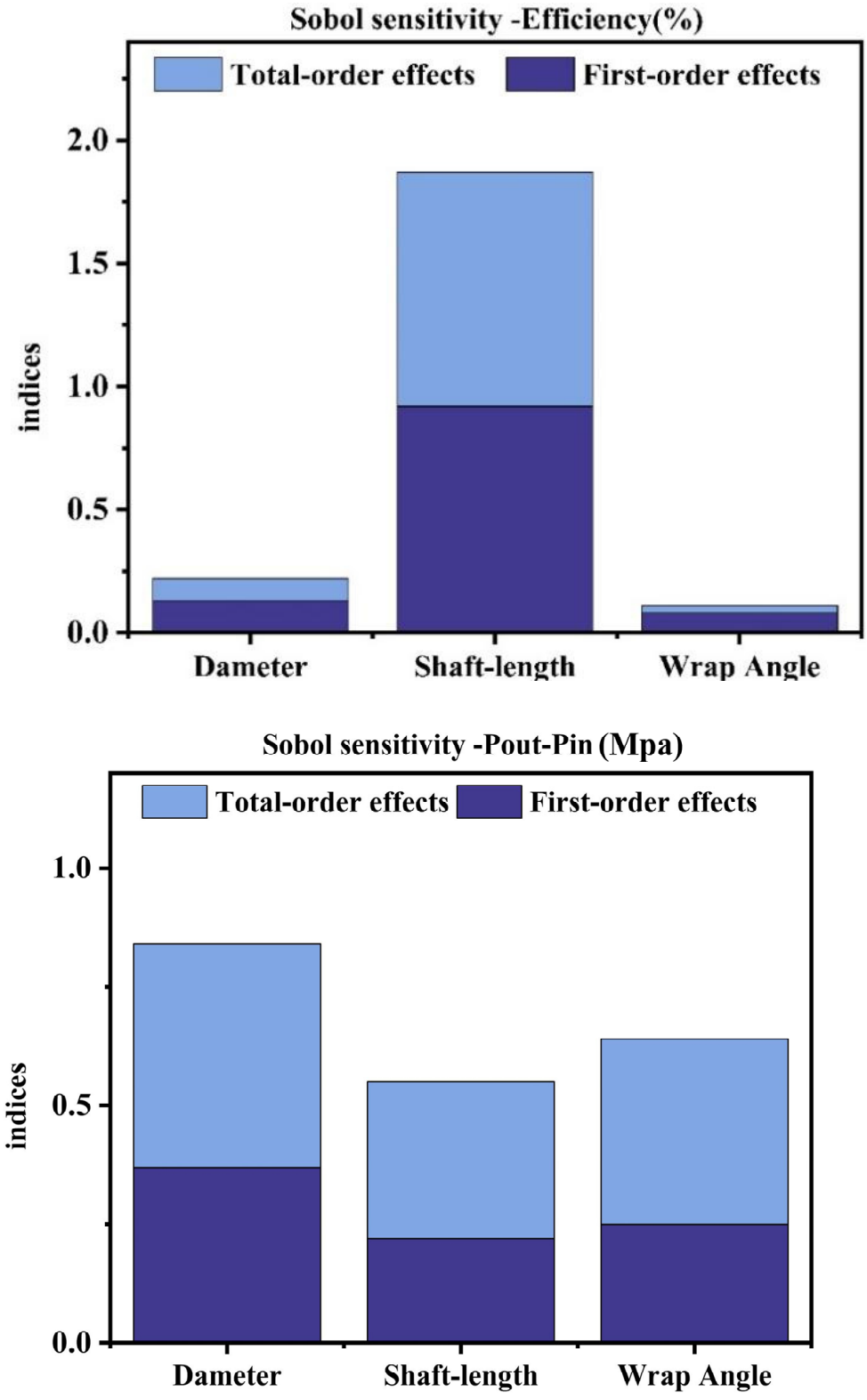


Figure 14. Sensitivity analysis results of the three dominant structural parameters on pressure rise and efficiency.

In contrast, the sensitivity patterns for efficiency differ markedly. The axial length exhibits a dominant influence on efficiency, with nearly overlapping first-order and total-effect indices (Si = 0.92, S_{Ti} = 0.95), indicating that efficiency is almost entirely governed by the independent effect of axial length, while interaction effects are negligible. The impeller outer diameter has a much weaker influence on efficiency (Si = 0.13), and its total-effect index (S_{Ti} = 0.09) is even lower than the first-order index. This counterintuitive result suggests that the influence of outer diameter on efficiency may be suppressed by interactions with other parameters. The blade wrap angle has an almost negligible impact on efficiency (Si = 0.08, S_{Ti} = 0.03), and can therefore be considered insignificant in terms of efficiency variation. These pronounced differences in parameter sensitivity indicate that pressure rise and efficiency respond to impeller geometric parameters through fundamentally different mechanisms. While pressure-rise performance is strongly affected by multi-parameter coupling effects, efficiency is predominantly controlled by axial length, highlighting the necessity of adopting different optimization strategies for these two key performance indicators.

Comprehensive analysis indicates that performance optimization of multiphase pumps requires differentiated parameter regulation strategies. For pressure-rise performance, priority should be given to optimizing the impeller outer diameter, which acts as the dominant parameter. Meanwhile, particular attention must be paid to the matching relationship between the blade wrap angle and other parameters, especially the axial length, since their synergistic effects play a critical role in pressurization. As a parameter with moderate influence, axial length can be optimized at a secondary stage for pressure-rise enhancement. In contrast, efficiency optimization is governed by a fundamentally different mechanism. Axial length is identified as the decisive parameter controlling pump efficiency and therefore requires focused optimization, whereas the effects of impeller outer diameter and blade wrap angle on efficiency can be considered negligible. This pronounced difference in parameter sensitivity provides a clear optimization pathway for practical design: first, ensuring an optimal axial length to achieve maximum efficiency; subsequently, adjusting the impeller outer diameter to satisfy pressure-rise requirements; and finally, exploiting the regulatory role of blade wrap angle to further enhance pressurization without compromising efficiency. Such a hierarchical and targeted parameter optimization strategy enables an effective overall improvement in multiphase pump performance. Based on the Sobol sensitivity analysis, the impeller outer diameter is identified as the most sensitive structural parameter affecting external performance, while the axial length exhibits the most moderate influence among the considered parameters.

8.2. Effects of Key Structural Parameters on the Internal Flow Characteristics of the Multiphase Pump

To further verify that the impeller outer diameter is the most influential structural parameter governing multiphase pump performance, this section compares the effects of the three dominant parameters on the internal flow characteristics of the pump, thereby validating the sensitivity analysis results. To clearly visualize the variations in internal flow induced by geometric parameter changes, nine representative cases are selected for post-processing analysis based on the baseline design parameters (D_0, e_0, θ_0) = (191, 50, 120), with dimensionless values (D/D_0, e/e_0, θ/θ_0) = (0.97, 1.00, 1.03).

Figure 15 illustrates the pressure rise distribution and blade loading at 0.5 blade height under different geometric configurations. As shown in the figure, among the three parameter variations, the baseline design exhibits a significantly smaller region of abrupt pressure increase (red regions) within the impeller compared with the other cases, while the corresponding pressure rise region within the diffuser is noticeably larger. This indicates that, under the design configuration, the impeller is able to convert mechanical

energy into fluid kinetic energy more effectively, which is subsequently transformed into pressure energy within the diffuser, resulting in superior pressurization performance. In contrast, for cases with reduced impeller outer diameter, the pressure gradient within the impeller passage becomes less pronounced. Similar trends are also observed for cases with reduced axial length and reduced blade wrap angle. However, for the small-diameter impeller, a relatively high-pressure region appears on the mid-span suction side of the blade and extends toward the central part of the flow passage. This phenomenon demonstrates that variations in impeller outer diameter have a significant influence on the internal pressure distribution and, consequently, on the pressurization performance of the multiphase pump.

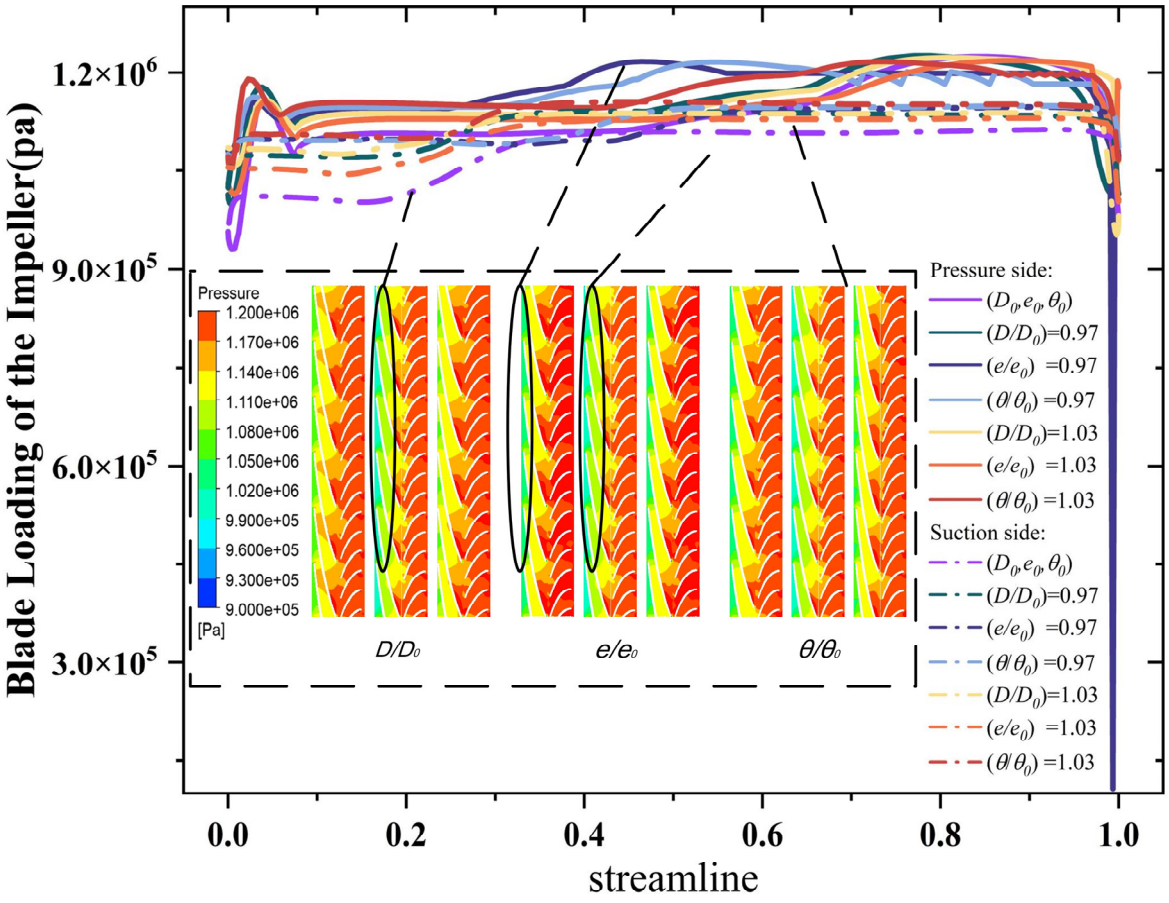


Figure 15. Pressure-rise distribution and blade loading at 0.5 blade height under different geometric configurations.

Figure 16 illustrates the gas streamlines at 0.5 blade height and the bar charts of inlet–outlet gas density difference (Δρ) under different geometric configurations. The results reveal a nonlinear response of Δρ to variations in the three structural parameters, namely D/D_0, e/e_0, and θ/θ_0. In general, a larger density difference indicates stronger gas compression or transport capability, implying that the gas acquires higher pressure energy through compression or kinetic energy conversion within the pump. Therefore, a higher Δρ corresponds to enhanced gas-handling performance. As shown in the figure, the gas streamlines inside the impeller are relatively uniform, with high inlet gas velocity. Within the impeller passages, the gas velocity first decreases and then increases, and a distinct recirculation region is observed near the impeller outlet. For variations in impeller outer diameter, large-diameter cases exhibit pronounced streamline bifurcation within the impeller passages, indicating the formation of low-gas-density regions. Meanwhile, the number

of vortices in the diffuser decreases, although their characteristic size becomes larger. In contrast, smaller-diameter cases show a greater number of vortices with smaller diameters.

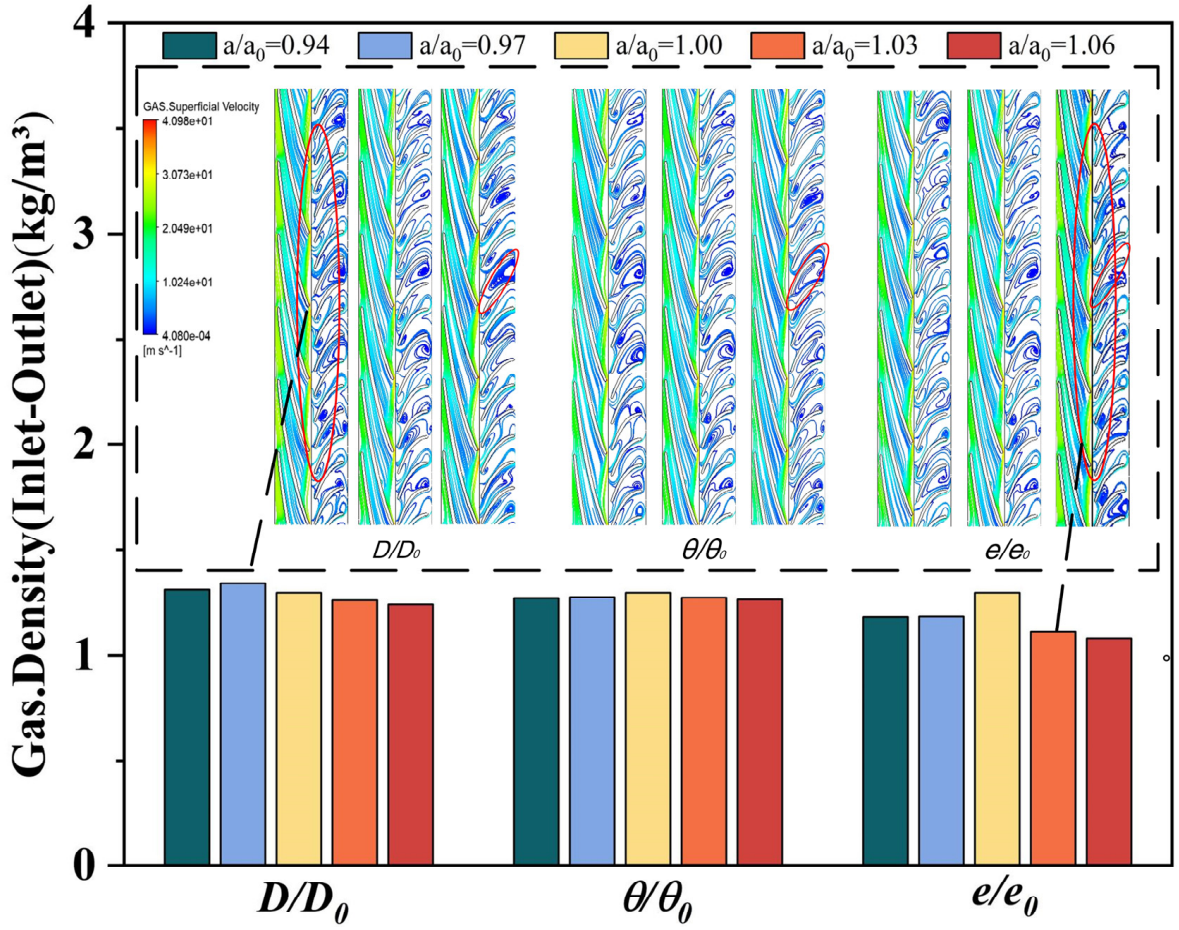


Figure 16. Gas-phase streamlines at 0.5 blade height under different geometric configurations and bar charts of inlet–outlet gas density variations.

For variations in blade wrap angle, no streamline bifurcation is observed in the impeller passage under large wrap angles; instead, this phenomenon shifts to cases with smaller wrap angles. Overall, the diffuser region exhibits the fewest gas vortices under the baseline design configuration, whereas both the number and size of vortices increased for the other two configurations. Notably, the largest gas vortices appear in the diffuser under large impeller outer diameter conditions, where they nearly occupy the entire diffuser passage. The gas density difference reaches its maximum at the baseline design parameters. On either side of this point, the performance variation exhibits clear asymmetry: when the dimensionless impeller outer diameter decreases, the reduction in $\Delta\rho$ is relatively gradual, whereas increasing the diameter leads to a much sharper decline. In particular, a cliff-like drop in $\Delta\rho$ is observed during the transition from 1.03 to 1.06, indicating the existence of a critical threshold for gas transport performance. Once this threshold is exceeded, the internal flow structure undergoes a fundamental change. The three structural parameters exhibit clear synergistic effects, with response trends generally consistent with those of the impeller outer diameter. The combined variation in impeller outer diameter, axial length, and blade wrap angle jointly governs the response of the gas density difference, resulting in complex nonlinear behavior. The performance curves remain relatively stable near the baseline range (0.97–1.03) but change significantly beyond this interval. These results demonstrate the highly sensitive and nonlinear response of gas transport performance to

geometric parameter variations, particularly under increasing parameter values, where rapid performance deterioration is observed.

It should be noted that variations in impeller outer diameter produce the smallest change in the inlet–outlet gas density difference, indicating that outer diameter has the weakest influence on gas transport capability among the three parameters, whereas blade wrap angle exerts the strongest effect.

Figure 17 presents the liquid-phase streamlines at 0.5 blade height and the corresponding bar charts of turbulent kinetic energy (TKE) within the impeller for different geometric configurations. Turbulent kinetic energy is a key indicator of flow stability and energy dissipation: higher TKE values imply more intense velocity fluctuations and a more disordered flow field, which can severely deteriorate gas–liquid transport efficiency.

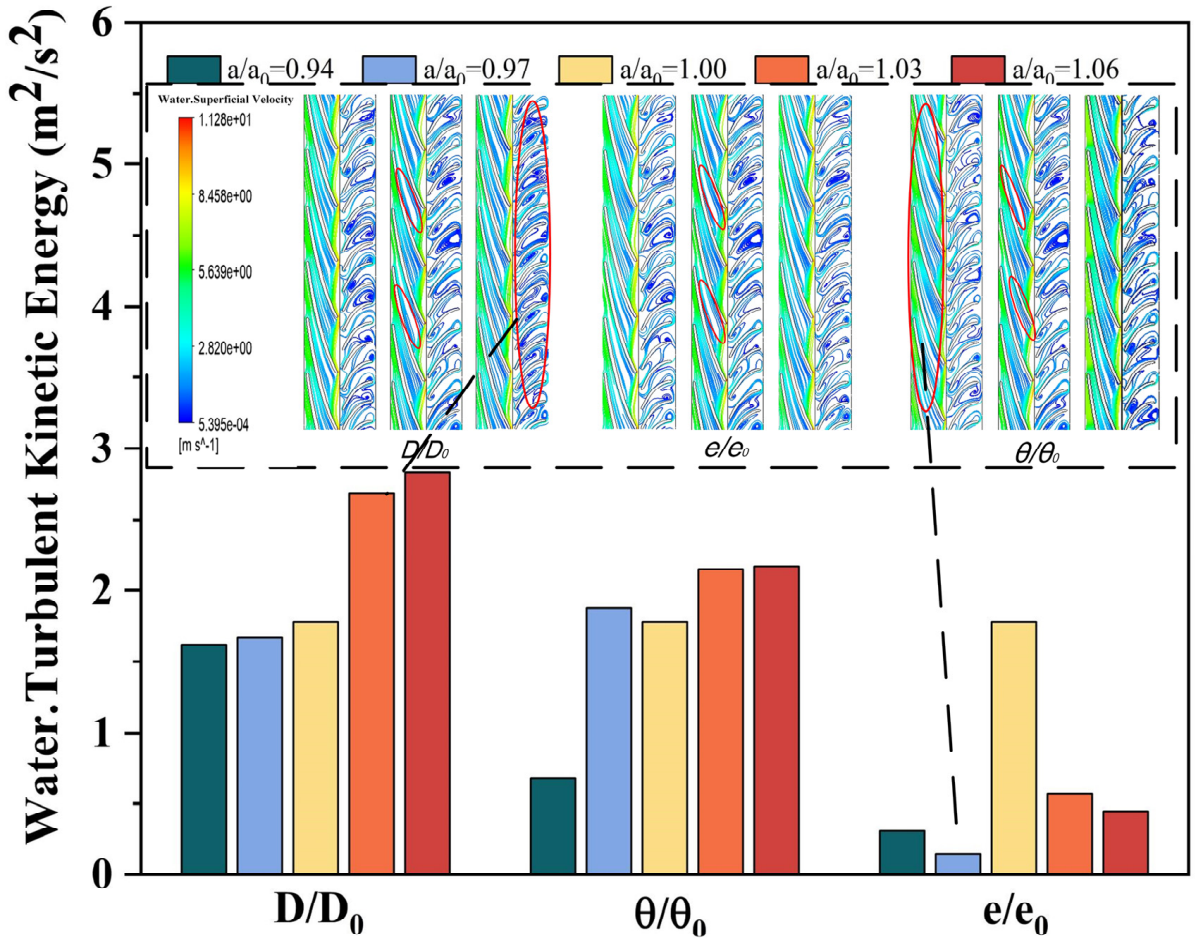


Figure 17. Liquid-phase streamlines at 0.5 blade height under different geometric configurations and bar charts of liquid-phase turbulent kinetic energy within the impeller.

As shown in the figure, the liquid-phase streamlines inside the impeller are relatively uniform, with high inlet velocities. Within the impeller passages, the liquid velocity first decreases and then increases, and the recirculation region near the impeller outlet is noticeably smaller than that observed for the gas phase. In addition, the distribution characteristics of liquid-phase streamlines differ significantly from those of the gas phase. Specifically, blank or low-velocity regions in the liquid-phase streamlines are mainly observed under the baseline design configuration, whereas such regions are almost absent under reduced or enlarged geometric conditions. In the diffuser region, the number of vortices formed by liquid-phase streamlines is substantially smaller than that of gas-phase vortices. Under the baseline design condition, liquid-phase vortices exhibit the largest characteristic diameter

but the smallest number, indicating that the liquid phase shows better adaptability to geometric variations than the gas phase. Among the three parameters, variations in impeller outer diameter exert the strongest influence on liquid-phase TKE within the impeller, while variations in blade wrap angle have the weakest effect. Comparisons of different impeller outer diameters reveal that larger diameters lead to a sharp increase in turbulent kinetic energy, suggesting that excessive outer diameter intensifies gas–liquid separation and secondary flow phenomena. As the diameter decreases, the reduction in TKE becomes relatively gradual. For axial length variations, extremely low TKE values are observed at small axial lengths ($e/e_0 = 0.96$), whereas TKE remains nearly unchanged when $e/e_0 \geq 0.97$. This indicates that shorter axial lengths effectively suppress the generation of turbulent kinetic energy, which is consistent with the fact that a reduced transport distance limits gas–liquid separation within the impeller. With respect to blade wrap angle, both large and small wrap angles contribute to a reduction in TKE, with smaller wrap angles exhibiting a more pronounced effect.

These characteristics reveal the complex response of liquid-phase turbulent kinetic energy to geometric parameter variations. The impeller outer diameter is identified as the most influential parameter affecting TKE magnitude, whereas blade wrap angle has the least impact. Moreover, shorter axial lengths and smaller wrap angles are shown to significantly reduce turbulent kinetic energy, thereby improving the liquid-phase transport capability of the multiphase pump.

Figure 18 illustrates the variation in liquid-phase vortex strength within the impeller under different geometric configurations, together with the vorticity distribution based on the Q-criterion. According to the Q-criterion definition $Q = \frac{1}{2}(\|\Omega\|^2 - \|S\|^2)$, vortex cores are identified as rotation-dominated regions where $Q > 0$. The dashed boxes from left to right represent the vortex distributions under the three structural parameter ratios of impeller outer diameter, blade wrap angle, and axial length, respectively.Horizontal comparisons show the evolution of vorticity distributions for different dimensionless values of the same geometric parameter. The bar charts quantify the nonlinear response of liquid-phase vortex strength to variations in the three structural parameters D/D_0, e/e_0, and θ/θ_0. The vortex strength (λ_{ci}) is a commonly used parameter in fluid mechanics for quantifying the local rotational intensity of vortical structures. It is defined as the imaginary part of the complex conjugate eigenvalues of the velocity gradient tensor ∇u, expressed as $\lambda = \lambda_{cr} \pm i\lambda_{ci}$. Physically, λ_{ci} represents the local angular rotation frequency of a fluid element; larger values indicate more concentrated rotational kinetic energy and more efficient local energy transfer. As shown in Figure 17, smaller impeller outer diameters correspond to the lowest vortex strength and smaller vortex core sizes, a trend that is also observed for reduced axial length and blade wrap angle. When the impeller outer diameter is increased, the vortex strength shows a decreasing tendency while the characteristic vortex diameter within the impeller slightly enlarges. For variations in axial length and wrap angle, smaller geometric values yield significantly higher vortex strength than other configurations, and vortex strength decreases progressively as the parameters increase. A notable difference is observed for axial length, where vortex strength drops sharply at first and then decreases more gradually. In contrast, for blade wrap angle, the minimum vortex strength occurs at the baseline design condition ($\theta/\theta_0 = 1.00$), with abrupt increases or decreases observed when moving from smaller to baseline values or from baseline to larger values. Overall, blade wrap angle exerts the strongest influence on impeller vortex strength and induces the most pronounced response, whereas the effect of impeller outer diameter is relatively weak and more gradual. In addition, increases in axial length and wrap angle promote an overall expansion of vortex structures, further indicating that

variations in impeller outer diameter play an important role in vortex generation and evolution within the multiphase pump.

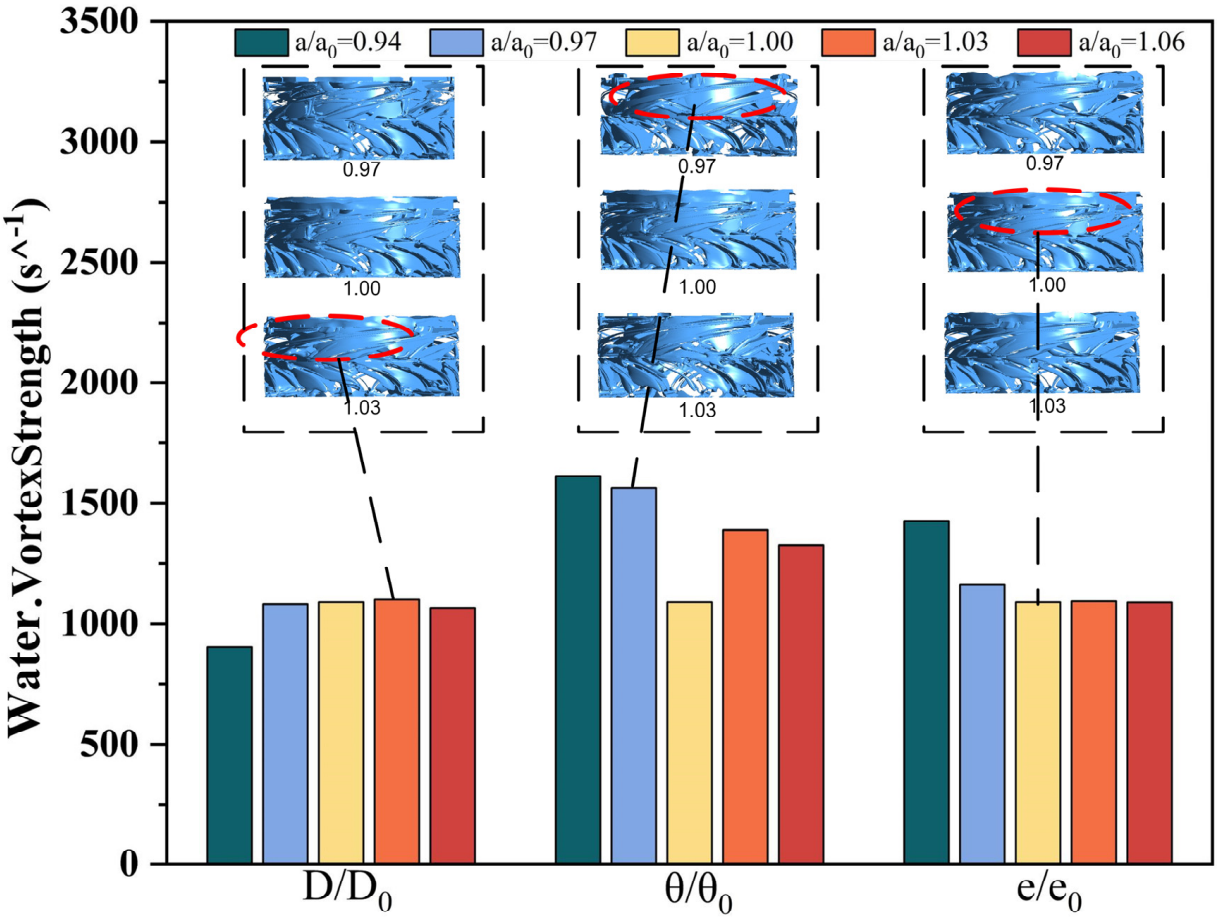


Figure 18. Variations in liquid-phase vortex strength in the impeller under different geometric parameters and vorticity distributions based on the Q-criterion.

It is worth noting that the variation trend of impeller vortex strength differs markedly from that of turbulent kinetic energy discussed previously. This discrepancy arises because, under conditions of high vortex strength, rigid-body vortices tend to dominate the flow. Such vortices exhibit a high degree of coherence, with fluid elements rotating synchronously within the vortex core and producing minimal velocity fluctuations. As a result, turbulent kinetic energy remains relatively low despite the presence of strong vortical structures.

8.3. Hierarchical Optimization Strategy for the Multiphase Pump

Figure 19 presents a comparison of the external performance among the optimal parameter combination, the worst parameter combination, and the baseline design using bar charts. The normalized values denote the ratios of efficiency and pressure rise relative to the baseline configuration. The yellow dashed line indicates the performance parameter at the design operating condition.

The results show that, under high gas volume fraction conditions, enhancing the performance of the multiphase pump requires a prioritized and hierarchical parameter optimization strategy. Specifically, the impeller outer diameter should be optimized first within the range of 183–191 mm to ensure sufficient pressure rise. Subsequently, the blade wrap angle should be constrained to 130–132° to achieve a balance between hydraulic efficiency and flow stability. Meanwhile, the axial length should be limited to $e \leq 44$ mm

to effectively suppress flow recirculation. Under these optimized conditions, the pump efficiency is increased by 6.8%, while the pressure-rise capability is improved by 12.3%.

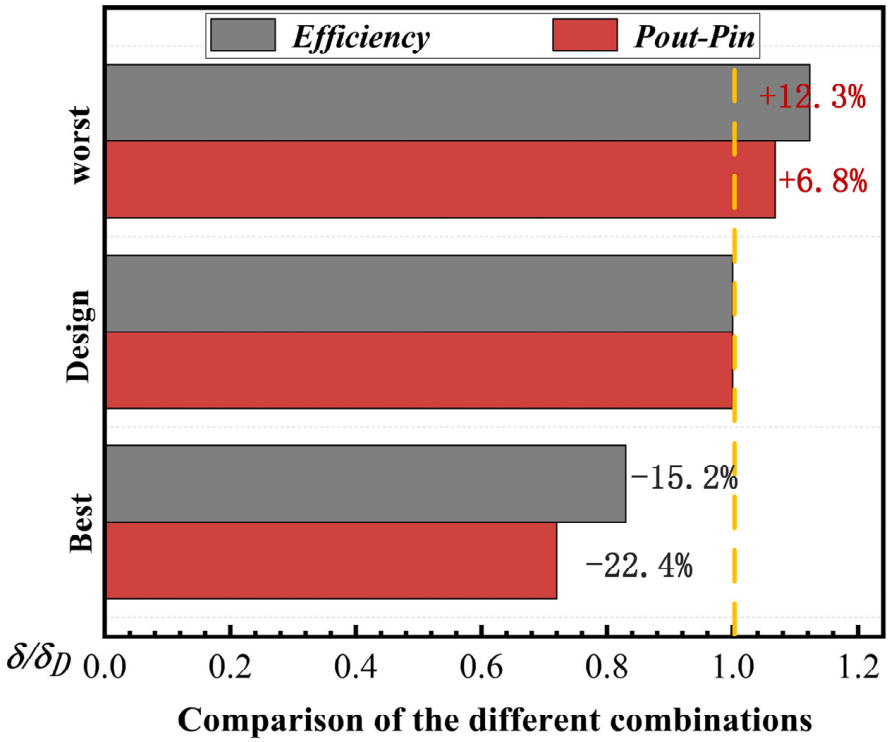


Figure 19. Performance comparison between the optimal parameter combination and the baseline design configuration.

In contrast, when the impeller outer diameter exceeds 211 mm, the blade wrap angle is reduced to 108–110°, and the axial length is greater than 56 mm, the pump performance deteriorates markedly. Under such unfavorable parameter combinations, the pressure rise decreases by 22.4% and the efficiency drops by 15.2% compared with the baseline design. These findings further demonstrate the effectiveness and necessity of the proposed hierarchical optimization strategy for multiphase pumps operating under high-GVF conditions.

9. Conclusions

In this study, a systematic sensitivity analysis of key impeller geometric parameters in a gas–liquid multiphase pump is conducted using the Morris screening method and Sobol global sensitivity analysis. Based on the obtained sensitivity hierarchy, an effective hierarchical optimization strategy is proposed. The main conclusions are summarized as follows:

(1) The impeller outer diameter is identified as the dominant parameter affecting multiphase pump performance and exhibits an approximately linear influence trend. Once the outer diameter exceeds the design value, pump performance deteriorates significantly. The blade wrap angle shows a clear threshold effect: when the wrap angle exceeds 120°, the pressure-rise performance declines rapidly while the sensitivity of efficiency decreases markedly beyond a wrap angle of 114°, indicating that excessively large wrap angles provide limited efficiency improvement. In contrast, the axial length exhibits conflicting effects on performance, showing a positive correlation with pressure rise but a negative correlation with efficiency. Shorter axial lengths are therefore favorable for efficiency enhancement.

(2) Combined sensitivity analysis and internal flow field investigations indicate that the optimal gas–liquid transport performance is achieved at the baseline design configuration. This result further confirms the reliability of the empirical design correlations commonly

adopted in multiphase pump design manuals and provides a solid theoretical basis for subsequent engineering designs.

(3) The impeller outer diameter has the weakest influence on vortex strength but exerts a strong impact on turbulent kinetic energy, indicating that diameter enlargement intensifies flow disorder and promotes turbulence development within the impeller passages. In contrast, blade wrap angle exhibits an opposite trend, as its variation reduces turbulent kinetic energy and promotes a more orderly flow structure. Moreover, the effects of impeller outer diameter and axial length on the inlet–outlet gas density difference are comparable and significantly stronger than that of blade wrap angle. This indicates that outer diameter and axial length play a more important role in gas transport capability, whereas blade wrap angle primarily contributes to improving liquid-phase transport performance.

Author Contributions: Methodology, G.S.; Software, Y.S.; Formal analysis, M.Z. and Y.S.; Investigation, P.L.; Resources, Y.S.; Data curation, M.Z. and P.L.; Writing—original draft, M.Z.; Writing—review & editing, G.S.; Visualization, M.Z. and Y.S.; Funding acquisition, G.S. All authors have read and agreed to the published version of the manuscript.

Funding: This research was funded by the Outstanding Youth Science Foundation of Sichuan Natural Science Foundation, grant number 2024NSFJQ0012; the Key Project of Regional Innovation and Development Joint Fund of the National Natural Science Foundation of China, grant number U23A20669; and the Sichuan Science and Technology Program, grant number 2022ZDZX0041. The authors have carefully checked the accuracy of the funding data and related information.

Institutional Review Board Statement: Not applicable.

Informed Consent Statement: Not applicable.

Data Availability Statement: The data presented in this study are available on request from the corresponding author.

Conflicts of Interest: The authors declare no conflict of interest.

References

1. Li, H.; Yang, J.; Zhang, W.; Hu, L.; Liang, A.; Yao, Z. Energy performance and unsteady gas-liquid flow characteristics of a multiphase rotodynamic pump: An experiment. *Appl. Energy* **2024**, *375*, 124112. [CrossRef]
2. Han, W.; Zhou, J.; Li, R.; Ma, X. Influence of trailing edge flap length and deflection angle on the performance of the multiphase pump. *Proc. Inst. Mech. Eng. Part A J. Power Energy* **2024**, *238*, 457–468. [CrossRef]
3. Li, Y.; Yu, Z. Distribution and motion characteristics of bubbles in a multiphase rotodynamic pump. *J. Pet. Sci. Eng.* **2020**, *195*, 107569. [CrossRef]
4. Shen, H.; Wen, X.; Trutnevyte, E. Accuracy assessment of energy projections for China by Energy Information Administration and International Energy Agency. *Energy Clim. Change* **2023**, *4*, 100111. [CrossRef]
5. Saldana, M.; Gallegos, S.; Galvez, E.; Castillo, J.; Salinas-Rodriguez, E.; Cerecedo-Saenz, E.; Hernandez-avila, J.; Navarra, A.; Toro, N. The Reynolds Number: A Journey from Its Origin to Modern Applications. *Fluids* **2024**, *9*, 299. [CrossRef]
6. Shi, G.; Liu, Z.; Xiao, Y.; Yang, H.; Li, H.; Liu, X. Effect of the inlet gas void fraction on the tip leakage vortex in a multiphase pump. *Renew. Energy* **2020**, *150*, 46–57. [CrossRef]
7. Shi, G.; Wang, S.; Xiao, Y.; Liu, Z.; Li, H.; Liu, X. Effect of cavitation on energy conversion characteristics of a multiphase pump. *Renew. Energy* **2021**, *177*, 1308–1320. [CrossRef]
8. Shi, G.; Yan, D.; Liu, X.; Xiao, Y.; Shu, Z. Effect of the Gas Volume Fraction on the Pressure Load of the Multiphase Pump Blade. *Processes* **2021**, *9*, 650. [CrossRef]
9. Shi, Y.; Zhu, H.; Yin, B.; Xu, R.; Zhang, J. Numerical investigation of two-phase flow characteristics in multiphase pump with split vane impellers. *J. Mech. Sci. Technol.* **2019**, *33*, 1651–1661. [CrossRef]
10. Zhang, J.; Tan, L. Energy Performance and Pressure Fluctuation of a Multiphase Pump with Different Gas Volume Fractions. *Energies* **2018**, *11*, 1216. [CrossRef]
11. Luo, X.; Zhang, W.; Li, C.; Yang, J.; Yao, Z. Unsteady flow analysis in a multiphase pump based on vorticity momentum density. *Results Eng.* **2024**, *24*, 103373. [CrossRef]

12. Dehghanghadikolaei, A.; Halim, B.A.; Khoshbakhtnejad, E.; Sojoudi, H. Dynamics of a Water Droplet IMpacting an Ultrathin Layer of Oil Suspended on a Pool of Water. *Fluids* **2024**, *9*, 82. [CrossRef]
13. Zhang, W.; Yu, Z.; Li, Y. Application of a non-uniform bubble model in a multiphase rotodynamic pump. *J. Pet. Sci. Eng.* **2019**, *173*, 1316–1322. [CrossRef]
14. Fagbade, A.; Heinz, S. Continuous Eddy Simulation vs. Resolution-Imposing Simulation Methods for Turbulent Flows. *Fluids* **2024**, *9*, 22. [CrossRef]
15. Liu, L.; Ahmed, U.; Chakraborty, N. A Comprehensive Evaluation of Turbulence Models for Predicting Heat Transfer in Turbulent Channel Flow across Various Prandtl Number Regimes. *Fluids* **2024**, *9*, 42. [CrossRef]
16. Safaei, S.; Mehring, C. Effect of Dissolved Carbon Dioxide on Cavitation in a Circular Orifice. *Fluids* **2024**, *9*, 41. [CrossRef]
17. Ma, X.; Zhang, Y.; Liu, X. CFD-based optimal design of rotor blades for an axial oil–gas multiphase pump. *J. Xihua Univ.* **2020**, *39*, 100–105.
18. Li, C. Mechanism of the Influence of Inlet Gas Volume Fraction on the Performance and Internal Gas–Liquid Two-Phase Flow Distribution of a Multiphase Pump. Ph.D. Thesis, Xi'an University of Technology, Xi'an, China, 2021.
19. Li, H.L. Optimization Design of Gas–Liquid Transport Performance for an Axial Multiphase Pump Based on Orthogonal Experimental Method. Master's Thesis, Xihua University, Chengdu, China, 2021.
20. Zhou, J.; Han, W.; Li, R.; Ma, X.; Wang, H.; Li, W. Flow Control in Multiphase Pumps Based on Separated Trailing Edge Flap. *Processes* **2023**, *11*, 3066. [CrossRef]
21. Han, W.; Zhang, J.; Xiao, M.Z.; Ma, X.N.; Qu, Z.; Yin, F.; Sun, Q. Influence of Bionic Waveform Leading Edge Blade on Drag Reduction Characteristics of Mixed Pump. *J. Appl. Fluid Mech.* **2023**, *16*, 920–931. [CrossRef]
22. Liu, M.; Tan, L.; Xu, Y.; Cao, S. Optimisation design method of multi-stage multiphase pump based on Oseen vortex. *J. Pet. Sci. Eng.* **2020**, *184*, 106532. [CrossRef]
23. Shi, G.T.; Yao, X.; Tao, S.; Sun, G.D. Effects of impeller blade number on the hydraulic performance of a multiphase pump. *J. Xihua Univ.* **2022**, *36*, 27–33.
24. Shi, G.T.; Zhao, Z.; Zhu, Z.; Zhou, M.H. Effects of diffuser blade number on internal energy loss in a multiphase pump. *Mach. Tool Hydraul.* **2022**, *50*, 91–93.
25. Erb, A.; Hosder, S. Analysis and comparison of turbulence model coefficient uncertainty for canonical flow problems. *Comput. Fluids* **2021**, *227*, 105027. [CrossRef]
26. Feng, K.; Lu, Z.; Yang, C. Enhanced Morris method for global sensitivity analysis: Good proxy of Sobol' index. *Struct. Multidiscip. Optim.* **2019**, *59*, 373–387. [CrossRef]
27. Barth, A.; Schwab, C.; Zollinger, N. Multi-level Monte Carlo finite element method for elliptic PDEs with stochastic coefficients. *Numer. Math.* **2011**, *119*, 123–161. [CrossRef]
28. Blatman, G.; Sudret, B. Efficient computation of global sensitivity indices using sparse polynomial chaos expansions. *Reliab. Eng. Syst. Saf.* **2010**, *95*, 1216–1229. [CrossRef]
29. Campolongo, F.; Saltelli, A. Sensitivity analysis of an environmental model: An application of different analysis methods. *Reliab. Eng. Syst. Saf.* **1997**, *57*, 49–69. [CrossRef]
30. Saltelli, A.; Annoni, P.; Azzini, I.; Campolongo, F.; Ratto, M.; Tarantola, S. Variance based sensitivity analysis of model output, Design and estimator for the total sensitivity index. *Comput. Phys. Commun.* **2010**, *181*, 259–270. [CrossRef]
31. Cheng, K.; Lu, Z.Z. Sparse polynomial chaos expansion based on DMORPH regression. *Appl. Math. Comput.* **2018**, *323*, 17–30. [CrossRef]
32. Borgonovo, E.; Plischke, E. Sensitivity analysis: A review of recent advances. *Eur. J. Oper. Res.* **2016**, *31*, 869–887. [CrossRef]
33. HTouhami, B.; Lardy, R.; Barra, V.; Bellocchi, G. Screening parameters in the Pasture Simulation model using the Morris method. *Ecol. Model.* **2013**, *266*, 42–57. [CrossRef]
34. Nabi, S.; Ahanger, M.A.; Dar, A.Q. Investigating the potential of Morris algorithm for improving the computational constraints of global sensitivity analysis. *Environ. Sci. Pollut. Res.* **2021**, *28*, 60900–60912. [CrossRef] [PubMed]
35. Miao, C.S. Working Theory and Design Method of Pressurization Units for Multiphase Pumps. Ph.D. Thesis, China University of Petroleum (East China), Dongying, China, 2007.

Disclaimer/Publisher's Note: The statements, opinions and data contained in all publications are solely those of the individual author(s) and contributor(s) and not of MDPI and/or the editor(s). MDPI and/or the editor(s) disclaim responsibility for any injury to people or property resulting from any ideas, methods, instructions or products referred to in the content.